University of Groningen

Gas and stellar dynamics in NGC 1068

Emsellem, E.; Fathi, K.; Wozniak, H.; Ferruit, P.; Mundell, C. G.; Schinnerer, E.

IMPORTANT NOTE: You are advised to consult the publisher's version (publisher's PDF) if you wish to cite from it. Please check the document version below.

Document Version
Publisher's PDF, also known as Version of record

Publication date:
2006

[Link to publication in University of Groningen/UMCG research database](#)

Gas and stellar dynamics in NGC 1068: probing the galactic gravitational potential

Eric Emsellem,[1]⋆ Kambiz Fathi,[2,3] Hervé Wozniak,[1] Pierre Ferruit,[1] Carole G. Mundell[4] and Eva Schinnerer[5]

[1]*CRAL-Observatoire, 9 avenue Charles André, 69231 Saint Genis Laval, France*
[2]*RIT Department of Physics, 84 Lomb Memorial Dr., Rochester, NY 14623-5603, USA*
[3]*Kapteyn Astronomical Institute, PO Box 800, 9700 AV Groningen, the Netherlands*
[4]*Astrophysics Research Institute, Liverpool John Moores University, 12 Quays House, Egerton Wharf, Birkenhead CH41 1LD*
[5]*Max-Planck-Institut für Astronomie, Königstuhl 17, 69117 Heidelberg, Germany*

ABSTRACT

We present SAURON integral field spectrography of the central 1.5 kpc of the nearby Seyfert 2 galaxy NGC 1068, encompassing the well-known near-infrared (NIR) inner bar observed in the K band. We have successively disentangled the respective contributions of the ionized gas and stars, thus deriving their two-dimensional distribution and kinematics. The [O III] and Hβ emission lines exhibit a very different spatial distribution and kinematics, the latter following inner spiral arms with clumps associated with star formation. Strong inward streaming motions are observed in both the Hβ and [O III] kinematics. The stellar kinematics also exhibit clear signatures of a non-axisymmetric tumbling potential, with a twist in both the velocity and Gauss–Hermite h_3 fields. We re-examined the long-slit data of Shapiro, Gerssen & van der Marel using a pPXF: a strong decoupling of the Gauss–Hermite term h_3 is revealed, and the central decrease of Gauss–Hermite term h_4 hinted in the SAURON data is confirmed. These data also suggest that NGC 1068 is a good candidate for a so-called σ drop. We confirm the possible presence of two separate pattern speeds applying the Tremaine–Weinberg method to the Fabry–Perot Hα map. We also examine the stellar kinematics of bars formed in N-body + smoothed particle hydrodynamics (SPH) simulations built from axisymmetric initial conditions approximating the luminosity distribution of NGC 1068. The resulting velocity, dispersion and higher order Gauss–Hermite moments successfully reproduce a number of properties observed in the two-dimensional kinematics of NGC 1068 and the long-slit data, showing that the kinematic signature of the NIR bar is imprinted in the stellar kinematics. The remaining differences between the models and the observed properties are likely mostly due to the exclusion of star formation and the lack of the primary large-scale oval/bar in the simulations. These models nevertheless suggest that the inner bar could drive a significant amount of gas down to a scale of ~ 300 pc. This would be consistent with the interpretation of the σ drop in NGC 1068 being the result of central gas accretion followed by an episode of star formation.

Key words: galaxies: evolution – galaxies: individual: NGC 1068 – galaxies: kinematics and dynamics – galaxies: nuclei – galaxies: Seyfert.

1 INTRODUCTION

The fuelling of active galactic nuclei (AGN) poses the problem of bringing gas into the close neighbourhood of the putative central dark mass, a supermassive black hole. Before reaching scales of a

few parsecs where turbulent viscosity becomes important (Wada & Norman 2002), the angular momentum of the gas must decrease by orders of magnitude. Quasi-stellar objects (QSOs) are usually associated with a major merging event that provides the necessary time varying potential to allow this to happen efficiently (Canalizo & Stockton 2001). However, the presence of a Seyfert nucleus does not correlate significantly with the presence of companions or other external environmental properties (Maia, Machado & Willmer 2003).

⋆E-mail: emsellem@obs.univ-lyon1.fr

In this context, departures from axisymmetry in the gravitational potential have been advocated to play an important contribution in the removal of angular momentum of the dissipative component (Heller & Shlosman 1994).

Quadrupole perturbations such as bars are ubiquitous in disc galaxies. Indeed, bars are good at redistributing the gas and more specifically at concentrating gas within their inner regions (Sakamoto et al. 1999). However, a correlation between the presence of a bar and the activity of the nuclear region is weak (Moles, Márquez & Pérez 1995; Mulchaey & Regan 1997; Malkan, Gorgian & Tam 1998; Knapen, Shlosman & Peletier 2000; Laine et al. 2002). This is not too surprising because the scales involved are very different: from the kiloparsec scale bars to the presumed central accretion disc. The bar-driven loss of angular momentum mainly occurs within the corotation radius (CR), leading the gas towards the inner resonances, e.g. the inner Lindblad resonance (ILR) if present, where the torques are cancelled out. Gas accumulates at this radius, forming an inner ring in which clumps of vigorous star formation are often observed (e.g. Schwarz 1981, 1984). The next step in moving gas to smaller radii is still under great debate. A number of processes, including secondary inner bars, inner spirals, lopsidedness and minor mergers (see Combes 2003, for a review) have been invoked, but none appears to provide a necessary and sufficient condition for the triggering of nuclear activity.

Although gas is a very sensitive tracer of the presence of a barred potential (e.g. Mundell & Shone 1999), its non-linear response to even weak non-axisymmetries means that it cannot be used directly to derive the gravitational potential of the galaxy. In addition, gas flows close to the AGN may be dominated by non-gravitational forces due to jets and outflow winds (Nelson & Whittle 1996). Therefore, the stellar kinematics, although challenging to measure in active galaxies, offer a more direct probe of the underlying potential.

The difficulty in making reliable measurements of the stellar kinematics in AGN, particularly in nuclear regions complicated by the presence of strong line emission, has resulted in only a limited number of moderate-resolution, stellar absorption line studies. Two-dimensional stellar kinematics have been published for only a small number of Seyferts (e.g. Arribas et al. 1997; García-Lorenzo et al. 1997; Arribas et al. 1999; Ferruit et al. 2004) and in some cases suffer from a too restricted field of view for accurate determination of the galaxy potential. For most Seyferts, only long-slit studies (Pérez et al. 2000; Emsellem et al. 2001; Filippenko & Ho 2003; Márquez et al. 2003) or central velocity dispersion measurements (Nelson & Whittle 1995, 1996) are available.

As one of the closest and most famous Seyfert 2 galaxies, NGC 1068 has been studied at most wavelengths and nuclear gas kinematics have been used to constrain its overall mass distribution. A good summarizing sketch of the observed components can be found in Schinnerer et al., (2000, S+00 hereafter, their fig. 6) where the outer disc and oval, the two-arm spiral and the near-infrared (NIR) bar are represented. The outer oval structure (with a diameter of 90 arcsec) has been interpreted by S+00 as a *primary* bar with $\Omega_p^P \sim 35$ km s^{-1} kpc^{-1}, consistent with the H I ring being at its outer Lindblad resonance (OLR) and the inner spiral arms seen in CO corresponding to its ILR. The NIR bar, which extends up to a radius of ~16 arcsec, would then be a *secondary* bar with an estimated pattern speed of $\Omega_p^S \sim 140$ km s^{-1} kpc^{-1}. This is consistent with the recent lower limit estimate of 135 ± 42 km s^{-1} kpc^{-1} derived by Rand & Wallin (2004, RW04 hereafter) based on an application of the Tremaine–Weinberg method (Tremaine & Weinberg 1984) using CO observations of the molecular gas. The same authors

argued for a different slower pattern speed for the CO spiral arms with $\Omega_p^S \sim 72$ km s^{-1} kpc^{-1}. However, based on the openness of the spiral arms, Yuan & Kuo (1998) argued these to be associated with the OLR of the inner bar. The only previous two-dimensional stellar kinematics study was achieved by García-Lorenzo et al. (1997) who obtained INTEGRAL spectroscopy (William Herschel Telescope; WHT) in the optical of the central 24 arcsec × 20 arcsec of NGC 1068. These authors suggest the presence of two puzzling kinematically decoupled stellar components in the central 10 arcsec, offset by about 2.5 arcsec from each other. Finally, Shapiro et al. (2003, Sh+03 hereafter) recently constrained the velocity dispersion ellipsoid of the disc using high-quality long-slit kinematics along the major and minor axes of the galaxy.

In this paper, we wish to further constrain the gravitational potential of NGC 1068 by mapping both its stellar and gas kinematics. We have thus used the integral field spectrograph Spectrographic Areal Unit for Research on Optical Nebulae (SAURON) to probe the region of the inner (secondary) bar. We report the results obtained from this data set, analysed with the help of N-body + SPH simulations. We first describe the SAURON observations and associated data reduction in Section 2. We then briefly present additional data we have gathered from different authors (Section 3) and present the results in Section 4. Numerical simulations for NGC 1068 are described in Section 5 and the resulting kinematics are then compared with our data. The results are discussed further in Section 6 and summarized in Section 7. Throughout this paper, we will use a distance of 14.4 Mpc for NGC 1068 (Bland-Hawthorn et al. 1997), leading to a scale of 69.8 pc arcsec^{-1}.

2 SAURON OBSERVATIONS AND DATA REDUCTION

2.1 The SAURON data cubes

We have observed NGC 1068 with the low-resolution (LR) mode of the integral field spectrograph SAURON during a run in 2002 January. SAURON delivers about 1500 spectra simultaneously, homogeneously covering a field of view of 41 arcsec × 33 arcsec with a squared sampling of 0.94 arcsec per spatial element (lens). The spectral domain and resolution are [4820–5280 Å] and 108 km s^{-1} ($\sigma_\star$), respectively. More details on the SAURON spectrograph can be found in Bacon et al. (2001), de Zeeuw et al. (2002) and Emsellem et al. (2004). The emission lines in NGC 1068 (particularly the [O III] lines) are so bright in the central part of NGC 1068 that the CCD saturates after about 8 min of exposure with the SAURON LR mode. We have therefore obtained a 5-min exposure to probe the central few arcseconds and three more exposures of 30 min to reach a sufficient signal-to-noise ratio at the edge of the field of view.

2.2 Data reduction with XSAURON

The data reduction of all four exposures was achieved using the dedicated XSAURON software and an automated pipeline available within the SAURON consortium (see Bacon et al. 2001; de Zeeuw et al. 2002, for details). The main steps include: removal of the CCD signature, extraction of the spectra using a mask built from an optical model of the telescope + spectrograph, wavelength calibration, low-frequency spectral fielding, cosmic rays removal, homogenization of the spectral resolution in the field, subtraction of the sky contribution using 146 dedicated lenses (1.9 arcmin away from the central field) and flux calibration. The sky spectra were carefully checked for

any significant contribution (emission/absorption) from NGC 1068 itself.

The flux-calibrated individual exposures are then accurately centred relative to each other using the associated reconstructed images and merged. Because the exposures are slightly offset from each other, we use the dithered data cubes to spatially resample the data cubes to 0.8 arcsec spaxel^{-1} (spatial pixel). Before merging, the spectra that exhibited saturated pixels were removed from the data cubes. This practically means that the spectra in the central 4 arcsec of the final merged data cube are only coming from the 5-min unsaturated exposure. At the edge of the SAURON field of view, the signal-to-noise ratio gets down to about 30 pixel^{-1}, sufficient for our goal of deriving the stellar kinematics.

2.3 Coordinate centring

We used the F547M Wide Field Planetary Camera 2 (WFPC2)/ *Hubble Space Telescope* [(*HST*), extracted from the European Southern Observatory (ESO) Space Telescope European Coordinating Facility (ST-ECF) archive] data to determine the relative spatial position of our SAURON data cube (see Fig. 1). Capetti, Macchetto & Lattanzi (1997) provided the absolute coordinate of the central peak of this optical image ($\alpha = 02^h42^m40\overset{s}{.}711$, $\delta = -00°00'47\overset{''}{.}81$, J2000, FK5, 80-mas accuracy), to be compared with the putative position of the central engine (CE) identified as the S1 radio source by Muxlow et al. (1996) at $\alpha = 02^h42^m40\overset{s}{.}7098$, $\delta = -00°00'47\overset{''}{.}938$. Taking S1 as our reference (0,0), we thus aligned the SAURON reconstructed image with the F547M WFPC2 exposure where the peak was assumed to be 0.13 arcsec north and 0.02 arcsec east of the CE (including a potential rotation of the SAURON field of view). This ensures an absolute positioning of our SAURON data cube on S1 with an error better than 0.1 arcsec in translation and than 0°.5 in rotation (the latter being dominated by the uncertainty on the relative angle between the WFPC2 and SAURON data). All maps
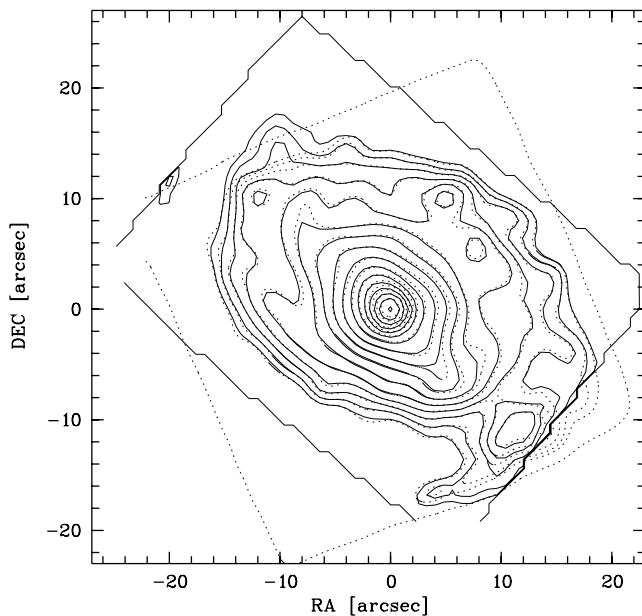

Figure 1. Isophotes (with steps of 0.5 mag arcsec^{-2}) of the central region as observed by SAURON (stellar continuum, solid lines) and with the WFPC2 camera aboard *HST* (F547M filter, dashed lines), after (seeing-)convolution by a gaussian of 2 arcsec. The agreement is excellent except at the border of the *HST*/WFPC2 field where edge effects due to the convolution are seen.

presented in this paper are oriented in the classical way, with north up and east left.

2.4 Stellar kinematics

The stellar contribution to the SAURON spectra is highly contaminated by strong emission lines: H$\beta\lambda$4861, the [O III]λ4959,λ5007 and [N I]λ5198,λ5200 doublets. We first identified the spectral regions that are significantly contaminated by emission. This required a detailed examination of the spectra in the merged data cube, particularly in the central 5 arcsec where the emission lines are very strong and wide. A first estimate of the stellar kinematics is then derived excluding the contaminated pixels. We achieve this by using a direct penalized pixel fitting routine (pPXF, Cappellari & Emsellem 2004): the algorithm finds the mean velocity V and velocity dispersion σ which minimizes the difference between the observed galaxy spectrum and the spectrum of a stellar template convolved by the corresponding gaussian (of mean V and root mean square σ). This is performed with the galaxy and template star spectra rebinned in ln λ. We use a single template star for this first estimate, namely the K2 giant HD 26162, also observed with SAURON. Best-fitting values for V and σ are thus obtained at each position (for each lens/spectrum) independently.

We then use this initial estimate of the stellar kinematics to derive an optimal stellar template for each individual spectrum. This is usually done using a large library of stellar templates. In the case of NGC 1068 and because of the significant number of pixels we had to exclude from the fit, this would make the fitting process strongly degenerate. We therefore decided to restrict our stellar library to include three different stellar templates from the single-age single-metallicity stellar population (SSP) models of Vazdekis (1999); this proved sufficient to properly fit the underlying stellar contribution (see Fig. 2). A multiplicative polynomial with a maximum degree of 6 was included in the fit in order to account for small residual differences between the stellar libraries and the SAURON spectra.

We finally iterate by measuring the velocity V and dispersion σ, as well as the third and fourth Gauss–Hermite moments h_3 and h_4 with the pPXF routine, this time using the optimal templates obtained from the previous step. h_3 and h_4 are indicators of the skewness and peakiness of the line-of-sight velocity distribution (relatively to a Gaussian). Although the signal-to-noise ratio per pixel (>30) is sufficient everywhere in the SAURON field of view to derive reliable h_3 and h_4 values, these should be taken with caution considering the limited spectral domain of the SAURON data cube, the medium spectral resolution of the SAURON spectra ($\sigma = 108$ km s^{-1}) and, more importantly, the contamination by bright emission lines. A comparison with long-slit data is helpful in this context (see Section 4.2).

2.5 Gas distribution and kinematics

The spectra resulting from the fitting procedure described in the previous section were subtracted from the original data to provide pure emission line spectra. The wavelength range of our observations includes the Hβ, [O III]$\lambda\lambda$4959,5007 and [N I]$\lambda\lambda$5198,5200 emission lines. These five lines are detected over our complete field of view, although the lines of the [N I] doublet were significantly weaker than the Hβ and [O III] lines and were barely detected in off-nuclear regions. The basic parameters of these emission lines (intensity, centroid velocity and velocity dispersion) were derived from Gaussian fitting of their profile using the FIT/SPEC software (Rousset 1992). When relevant, the lines were constrained to have
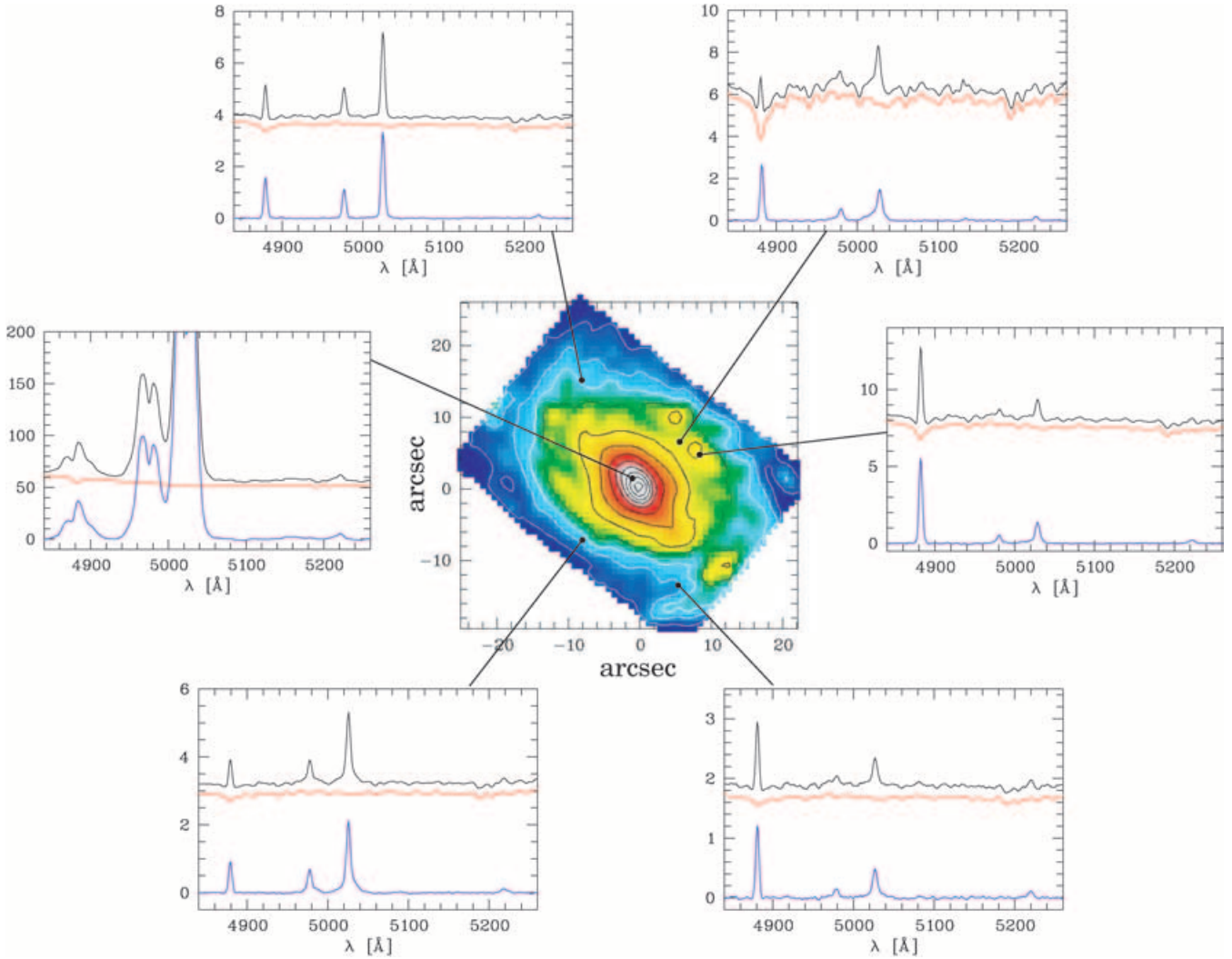
Figure 2. Fits of the SAURON spectra of NGC 1068 using the Vazdekis (1999) stellar library. Six spectra (black lines) and their corresponding fits (red lines) at different locations in the SAURON field are shown, the individual spatial locations being indicated by arrows on the reconstructed intensity SAURON map. The vertical positions of the best-fitting spectra are arbitrarily shifted for legibility, the residual spectra being presented in the same panels (blue lines). The SAURON map has north up and east left.

fixed or bounded ratios ([O III]λ5007/[O III]λ 4959 = 2.88; 0.7 < [N I]λ5198/[N I]λ 5200 < 2.0).[1] To stabilize the fit of the weak [N I] lines, we forced them to share the same velocity and width as the Hβ line.

Careful examination of the spectra showed the presence of several kinematically distinct components in the profiles of the Hβ and [O III] emission lines, in agreement with the results of Arribas, Mediavilla & García-Lorenzo (1996) and García-Lorenzo et al. (1999). In our data, we have identified three different systems, which follow.

(i) A first component, which is observed everywhere in our field of view. It is relatively narrow (typical dispersion of 100 km s^{-1} or lower beyond 5 arcsec from the nucleus) everywhere except in the nuclear regions and it is therefore termed 'narrow' hereafter. Despite its broadening in the nuclear region and the presence of the other

systems, it is possible to follow this 'narrow' component down to about 2 arcsec from the centre.

(ii) A broad (dispersion higher than 600 km s^{-1}), blueshifted component (hereafter termed 'broad'), which is observed up to 8–10 arcsec from the nucleus and often appears as a blue wing in the [O III] line profile (see, e.g., panel 4 of Fig. 3).

(iii) A very spatially localized, intermediate-dispersion component (hereafter termed 'additional') observed in the vicinity of the nucleus and either strongly blueshifted (north-east of the nucleus) or redshifted (south-west of the nucleus, see e.g. panels 2 and 3 of Fig. 3) with respect to the systemic velocity of the galaxy.

Examples of spectra displaying these three kinematic components are shown in Fig. 3, which can be compared with fig. 7 in García-Lorenzo et al. (1999). Our narrow, broad and additional components correspond to components (1), (2) and (3), and (4a) and (4b), respectively, in García-Lorenzo et al. (1999). In our data, it was not possible to disentangle their components 2 and 3. This is probably due to our spatial sampling (0.8 arcsec per lens), which makes it difficult to study the (complex) central few arcseconds where

---

[1] Range estimated using the MAPPINGS IC software with an electronic temperature of 10^4 K and electronic densities from 0.1 to 1000 cm^{-3} (Ferruit et al. 1997).
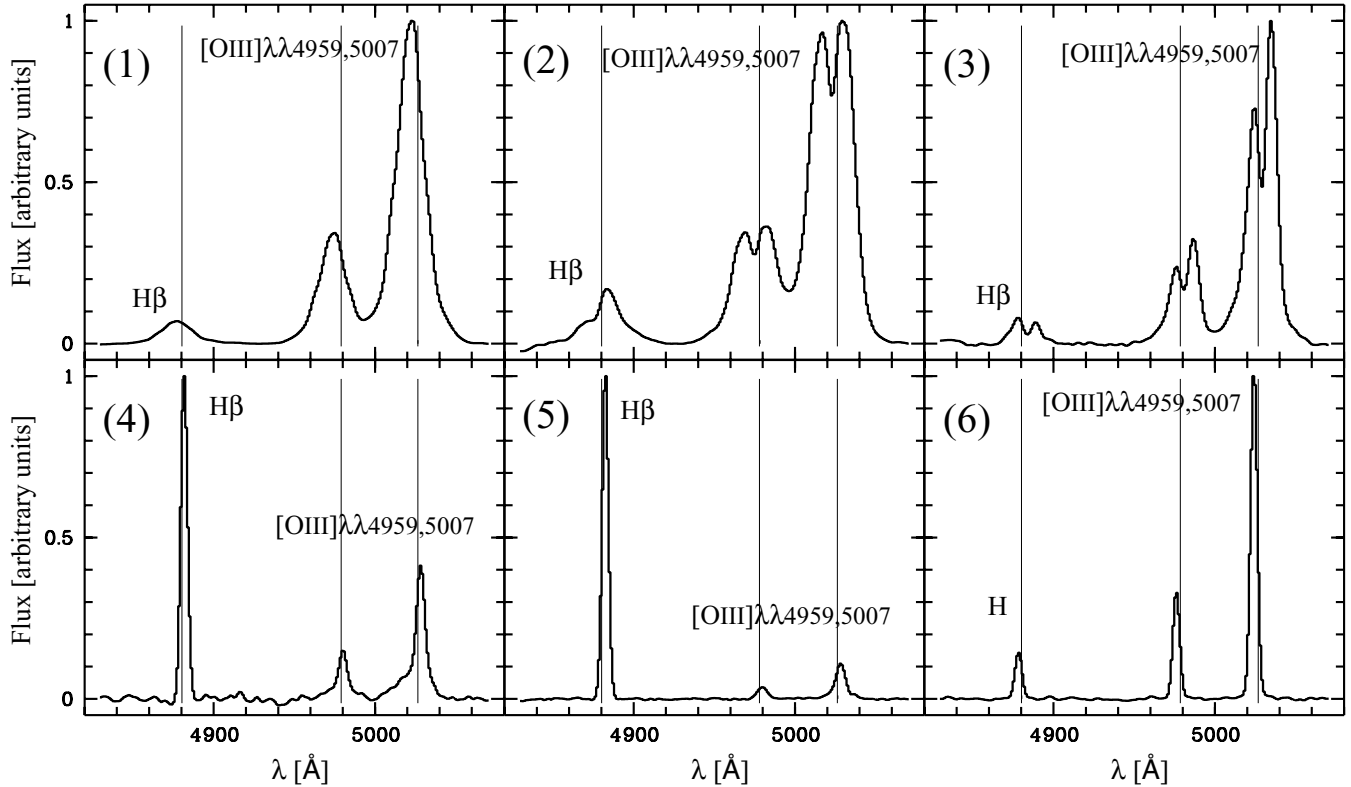
Figure 3. Examples of spectra of NGC 1068 obtained with SAURON. The spectra, normalized to a peak intensity of unity, have been truncated to show only the wavelength range including the Hβ and [O III]$\lambda\lambda$ 4959,5007 lines. The dotted vertical lines indicate the expected position of a line at rest in the galaxy frame (systemic velocity of 1144 km s^{-1}). (1) Nuclear spectrum. (2) and (3) Spectra located at positions ($-1.3,+1.2$ arcsec) and ($+0.5,-2.8$ arcsec) where both the narrow and additional components are present. In panel (2), the narrow component is redshifted with respect to the systemic velocity (the additional component being blueshifted), whereas in panel (3) it is the opposite. (4) Spectrum located at ($+5.3,+8.4$ arcsec) in which both the narrow and broad components are present in the [O III] lines. (5) and (6) Spectra located ($+13.3,-6.8$ arcsec) and ($-16.3,+14.8$ arcsec), respectively, and in which only the narrow component is observed (but with very different [O III]λ4959/Hβ ratios).

component (3) is identified by these authors. For the same reasons, conducting a similar comparison with the decomposition used by Arribas et al. (1996) proved very difficult because their observations cover only the nuclear regions (see their section 3.2.1). It must also be emphasized that each system identified in the SAURON spectra may itself result from a blend of separate (and unresolved) velocity systems: this is, for instance, clearly the case in the central few arcseconds (Cecil et al. 2002).

At distances >5 arcsec from the nucleus (corresponding to 1822 spectra out of a total of 1943), the line profiles were simple enough for an automated fit to be conducted. The various maps inferred from the results of this automated fit were carefully checked and only a small number of spectra had to be fitted individually a second time. In contrast, the automated fit to spectra in the inner regions (radii less than 5 arcsec) was unstable, as expected. All spectra had to be examined and fitted individually and, quite often, additional constraints (especially on the width of the broad and additional components) were imposed. Our results in these inner regions (which, however, represent only a small fraction of our field of view) are therefore less reliable than those for the outer regions.

Given the known kinematic complexity of the nuclear regions (Cecil, Bland & Tully 1990) and the limitations of our data set in this region, we do not discuss the properties of the additional and broad components further. In the following, we focus on the properties of the narrow component, which is more representative of the underlying galaxy.

Errors on the emission line parameters were derived by use of Monte Carlo realizations repeating the fitting procedure 500 times using simulated emission line spectra. These were built as the sum of a synthetic noise-free spectrum (with spectral characteristics typical of the observed spectra) and noise. Additional errors on the centroid velocities (18 km s^{-1} for 3σ calibration errors) and the full width at half maximum (FWHM, 0.1-Å peak to valley for variations of the 'instrumental' FWHM over the field of view) were included in the final error budget. In the case of the centroid velocities of the narrow component, the contribution of the fit to the total error was negligible for spectra dominated by this component (i.e. typically at radii > 5 arcsec) and with a peak signal-to-noise ratio larger than 10 (i.e. over most of our field of view): the overall accuracy on the measured centroid velocity is then better than 20 km s^{-1}.

3 ANCILLARY DATA SETS

In this section, we briefly describe ancillary data sets we use in this work, namely some optical and NIR images as well as the H I velocity rotation curve for the dynamical modelling (Section 5), Hα, and CO distribution and kinematics for comparison with our emission line SAURON maps.

3.1 Ground-based photometry

A deep *B*-band image was used to probe the outer disc of NGC 1068 up to a radius of 200 arcsec. This image was obtained

with the 1-m telescope on Mount Laguna (Cheng et al. 1997) and is a combination of three exposures of 300 s each. It has a field of view of about 800 arcsec sampled at 0.4 arcsec pixel^{-1}. We also made use of the Digitized Sky Survey (DSS) *I*-band (available via the ESO/ST-ECF archive: http://archive.eso.org/) and Two Micron All Sky Survey (2MASS) *K*-band images, both having a scale of about 1 arcsec pixel^{-1}. Finally, a high-resolution *K*-band image was obtained by Peletier et al. (1999): this has a pixel size of 0.248 arcsec, a field of view of about 1 arcmin^2 and a seeing of 0.5 arcsec (FWHM).

3.2 H I velocity curve

The H I velocity curve we used has been published in the Ringberg Standards (RS hereafter, Bland-Hawthorn et al. 1997) from the work of Brinks et al. (1997). It comprises measurements up from the centre to about 200 arcsec, the last radius at which Brinks et al. (1997) detected the low surface brightness H I disc. The H I rotation curve decreases from about 130 km s^{-1} at 30 arcsec to 95 km s^{-1} at 180 arcsec from the centre.

3.3 The Hα distribution and kinematics

Dr J. Bland-Hawthorn provided us with the Hα Fabry–Perot data as published in Bland-Hawthorn, Sokolowski & Cecil (1991), including the luminosity and mean velocity maps. The data cube was obtained with the Hawaii Fabry–Perot Interferometer (HIFI) at the Canada–France–Hawaii Telescope (CFHT; Mauna Kea). The velocity resolution was 65 km s^{-1}, the spatial sampling and resolution (FWHM) being 0.43 and 0.8 arcsec, respectively. The Hα velocity field was published in Dehnen et al. (1997).

3.4 The CO distribution and kinematics

We also make use of the high-resolution CO interferometric data published in S+00. This ^{12}CO(1–0) data set has been obtained with the Institut de Radio-Astronomie Millimétrique (IRAM) millimeter interferometer on the Plateau de Bure (France), providing a circular beam of 1.4 arcsec (sampling of 0.4 arcsec), with a channel width of 10 km s^{-1}. Apart from a central ring-like structure, the molecular gas is mainly distributed along a two-arm spiral that is just outside

the inner NIR bar and is associated with the ILR of the outer oval (S+00).

3.5 Long-slit stellar absorption kinematics

Finally, we include results from long-slit spectroscopy conducted by Sh+03 who kindly made the fully reduced data sets available to us: stellar kinematic profiles along the major and minor axes of the galaxy (position angles, PAs, of 80° and 170°) were obtained with a slit width of 3 arcsec centred on the Mgb triplet around 5175 Å. The stellar kinematics published in Sh+03 were obtained using a Fourier fitting algorithm. In this paper, we re-analysed these data favouring the pPXF routine as it allows an optimal selection of regions uncontaminated by emission lines and to derive robust estimates of moments up to h_3 and h_4. We have only included wavelengths between 5237 and 5549 Å to avoid contamination from the very bright emission lines present in these spectra of NGC 1068.

4 DATA ANALYSIS

4.1 Morphology and position angles

In this section, we derive new values for the main morphological parameters of the different components of NGC 1068 (bar, oval, outer disc), because these are important parameters when comparing different data sets and models. A schematic summarizing the structures observed in NGC 1068 is provided in Fig. 4.

We first wish to re-examine the PA and ellipticity of the outer disc. The RS quote a value of 106° ± 5°, which in fact corresponds to the average PA of the *kinematic* axis as fitted on the large-scale H I data (Brinks et al. 1997). The total H I surface brightness in the outer disc (100–200 arcsec) is rather low and exhibits a north/south asymmetry at its outer edge (lower surface brightness in the south). At this radius, the stellar component is easily observed using the DSS *I*-band image: outside 190 arcsec, there is a clear mildly flattened component with a PA between 74°.5 and 84°, therefore at least 20° from the kinematic PA measured in H I. A value of 80° ± 5° is consistent with the optical and smoothed H I surface brightness shown in Dehnen et al. (1997) and we will adopt this value as the apparent photometric PA of the outer disc, thus different from the H I kinematic PA. The axis ratio of the best-fitting ellipse of the optical outer disc is between 0.8 and 0.85.
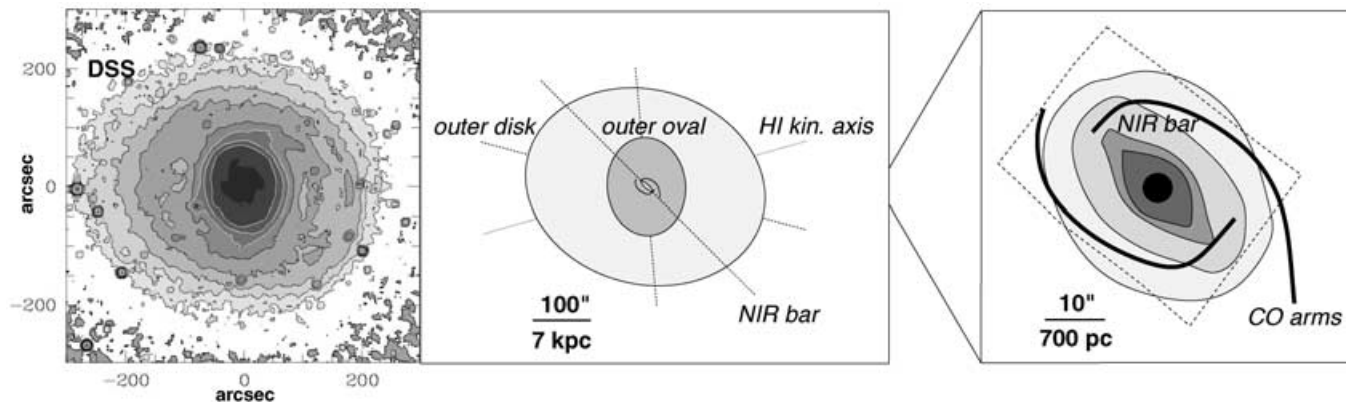

Figure 4. Schematic of the structures observed in NGC 1068. Left panel: 10 arcmin × 10 arcmin DSS *I*-band image. The central 40 arcsec is saturated. Isophotes are shown with a step of 0.5 mag arcsec^{-2}. Middle panel: sketch at the same scale as the DSS image. The major axes of the outer disc, outer oval and inner near-infrared bar are indicated (dashed lines). The H I kinematic axis is shown as a dotted line for comparison. Right panel: zoomed sketch (×10) showing the location of the near-infrared bar and the CO arms (see Schinnerer et al. 2000, figs 1 and 6). The extent of the SAURON field of view is indicated by a dashed polygon.

We then remeasured the characteristics of the outer oval and NIR bar using ellipse fitting. Both the DSS *I*-band and the *B* deep images lead to a radius of 90 arcsec, an axis ratio of 0.8 and a PA of 5° for the outer oval, perfectly consistent with the RS values. Using our high-resolution *K*-band image, we find an average PA of $44°5 \pm 0°5$ for the NIR bar (between a 10- and 16-arcsec radius), as compared with the RS value of $48° \pm 2°$ (from Scoville et al. 1988). Our value is, however, consistent with the one provided by Thronson et al. (1989) of $45°0 \pm 0°5$. In the following, we will therefore use an average value of $44°5$. The minimum axis ratio is 0.45 at a radius of 15.5 arcsec.

4.2 Stellar kinematics

The SAURON stellar kinematics are presented in Fig. 5. Inside the central 4 arcsec, the measurements are significantly perturbed due to the emission line contamination and should be taken only as indicative. The stellar velocity field clearly exhibits strong departures from axisymmetry, with an S-shaped zero velocity curve and the line of maximum velocity having a changing PA. The amplitude of the velocity field reaches ~ 115 km s^{-1} at a radius of about 10 arcsec. We wish to draw attention to a small perturbation of the order of 20 km s^{-1} at the south-east edge of the field (absolute values

being smaller, around a band going from 12 arcsec east, 6 arcsec south to -18 arcsec east from the nucleus; see Section 4.3) and a similar trend is mirrored on the opposite side. The velocity dispersion map shows a rise towards the centre with $\sigma \sim 60$ km s^{-1} at 20 arcsec from the centre along the major axis and between 100 and 200 km s^{-1} in the central 10 arcsec. There is a slight asymmetry in the dispersion map (dispersions being higher by ~ 20 km s^{-1} on the western side of the field), probably the result of a residual gradient of the spectral resolution over the field of view: however, this does not affect our conclusions. The h_3 map displays a significant change of sign from the south-east quadrant to the north-west quadrant. The structure of positive and negative h_3 is roughly elongated along the PA of the NIR bar. There is an elongated ring-like region of positive values in the h_4 map (with maxima around 0.06–0.1 between radii of 8 and 12 arcsec) and a depression inside a radius R of 8 arcsec with h_4 going slightly negative. We cannot however follow this inward decrease of h_4 for $R < 4$ arcsec because of the emission-line contamination.

We now compare the kinematics published by Sh+03 and obtained via a Fourier fitting technique, with our reanalysis of the same data set using pPXF (Fig. 6). The central velocity dispersion does not peak so clearly in the profiles re-extracted from the Sh+03 data: we were unable to reproduce the high central σ value even
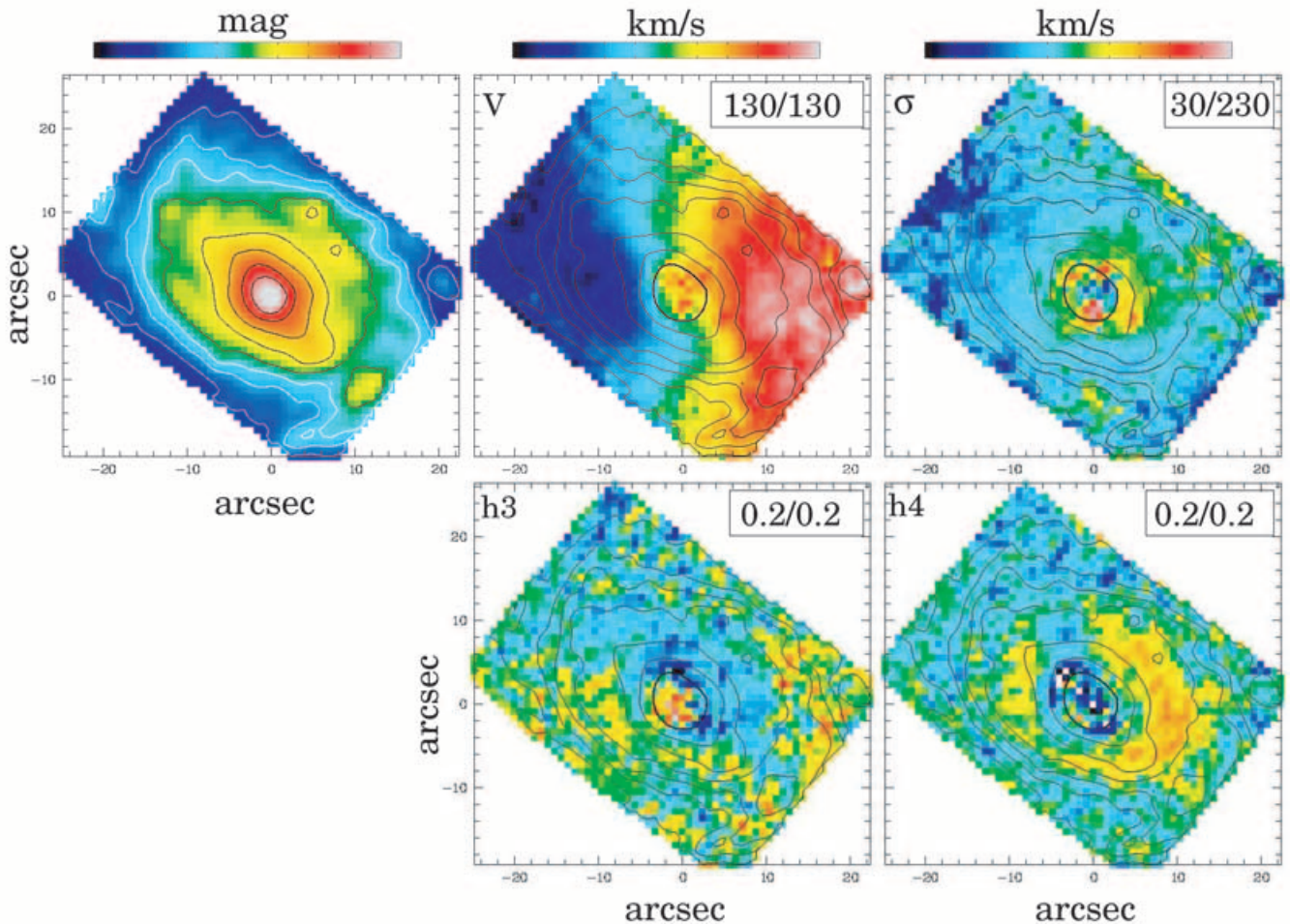
Figure 5. Reconstructed maps of the stellar kinematics of NGC 1068 obtained from the SAURON data cube. From left to right: intensity, velocity *V*, velocity dispersion σ (top panels), and higher order moments h_3 and h_4 (bottom panels). The thick contour approximately marks where the kinematic measurements are very significantly perturbed by the presence of very strong and wide emission lines. Boxes in the top right corner of the panels show the ranges covered by the colour bars.
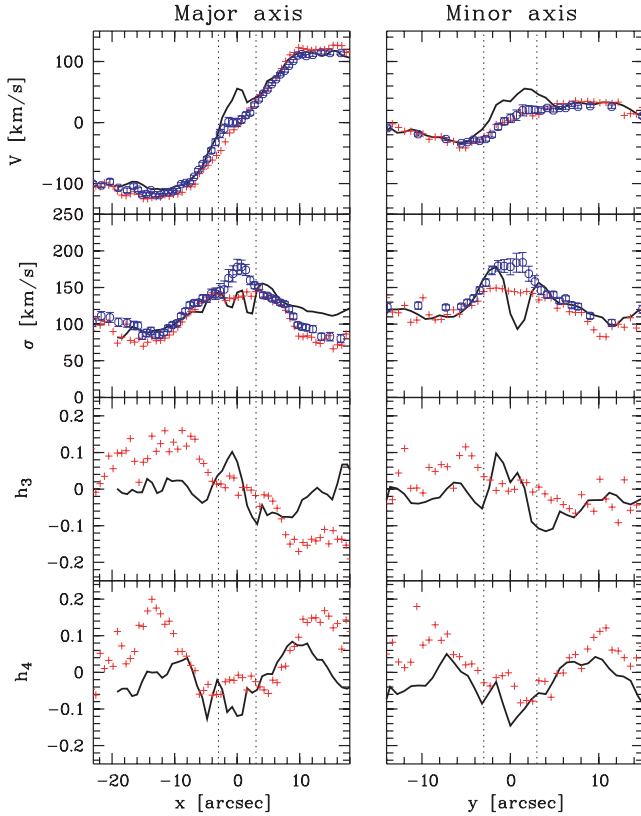
Figure 6. Comparison between stellar kinematic profiles extracted from the SAURON (solid lines) and Sh+03 (crosses). From top to bottom: mean velocity, velocity dispersion, h_3 and h_4. The SAURON data have been averaged over a slit width of 3.2 arcsec (the central 3 arcsec are unreliable due to the presence of dominating emission lines). The mean velocity and dispersion profiles originally published by Sh+03 are provided as circles (with error bars). The 'major axis' here corresponds to PA = 80° and the 'minor axis' to PA = 170°.

by changing our stellar template or spectral domain. There is also a slight flattening of the major-axis velocity gradient in the central 2 arcsec in the Sh+03 profiles, which we do not see in our measurement. The h_3 profiles are anticorrelated with V with peak values of ± 0.15 around 10 arcsec along the major axis. The h_4 profiles exhibit a significant depression in the central 5 arcsec with a negative minimum of ~ -0.04 at the centre. The maximum value of h_4 is reached at a radius of about 14 arcsec along the major axis and 10 arcsec along the minor axis confirming the elongation of this ring-like structure. The presence of a drop in the central dispersion profile is confirmed by Shapiro & Gerssen (private communication) who re-examined this data set and applied their own pixel fitting routine. We presume that the central peak in the stellar velocity dispersion observed in Sh+03 is due to the influence of the strong [N I] doublet when using a Fourier fitting program to extract the kinematics. Considering this reanalysis, NGC 1068 is therefore a new candidate for the presence of a so-called σ drop (Emsellem et al. 2001; Márquez et al. 2003; Wozniak et al. 2003).

Overall, the SAURON stellar kinematics averaged over a reconstructed slit of 3.2-arcsec width compare reasonably well with the published long-slit data of Sh+03, although there are significant discrepancies worth mentioning: the SAURON dispersion values are too high on the western side of the major axis, confirming the fact that the SAURON data have a residual spatial variation of the

spectral resolution. In contrast to the profiles measured from the Sh+03 data, our h_3 data do not show a significant gradient. This is primarily due to our lower spectral resolution ($\sigma = 108$ km s^{-1}, as compared with about 30 km s^{-1} for Sh+03), which obviously also affects our h_4 measurements.

We do not see any hint of the decoupled kinematic structure claimed by García-Lorenzo et al. (1997, 1999). Although the derived stellar kinematics within the very central 4 arcsec are unreliable, we should be able to detect the presence of a large east–west velocity gradient as implied by the pinched isovelocities in the maps of García-Lorenzo et al. (1997). There is also no hint of an abrupt velocity change in the minor-axis kinematics of Sh+03. This strongly suggests that the kinematic structure observed by García-Lorenzo et al. (1997, 1999) is an artefact in the INTEGRAL/WHT data.

4.3 Gas distribution and kinematics

The maps of the distribution and kinematics of the Hβ and [O III] components, as reconstructed from the results of multiple Gaussian fits to the data, are displayed in Fig. 7.

Hβ emission from the narrow component is ubiquitous in our field of view, but the brightest region corresponds to the inner 3 arcsec of the galaxy. Away from these nuclear regions, the narrow-component Hβ emission is dominated by the contribution from the spiral arms. The distribution of Hβ shows the known northern and southern spiral arms, although they seem almost connected at this resolution. Comparison between the total (all kinematic components included) and narrow-component-only Hβ maps (top left panels of Fig. 7) shows little difference between the two maps outside of the nuclear regions, outlining the fact that the narrow component dominates the Hβ emission away from the nucleus.

As for Hβ, emission from the inner 3 arcsec of the galaxy also dominates the narrow-component [O III] map. However, away from the nucleus, the distribution of the [O III] emission differs significantly from the distribution of the Hβ one. The distribution of the [O III] emission is very asymmetric, thus found predominantly northeast of the nucleus, and does not trace the spiral arms. Instead, it traces the northern ionization cone (see e.g. Pogge 1988).

Despite the differences between the distribution of Hβ and [O III], the overall morphologies of the Hβ and [O III] velocity fields (see Fig. 7) are very similar. They both display the prominent S-shaped structure, which is already present in the data of Cecil et al. (1990; see also Section 4.4) and of García-Lorenzo et al. (1999, their fig. 16). However, if we take a closer look at these velocity maps, we see differences between the observed [O III] and Hβ velocities in some regions. We have therefore built a map of $v([O III]) - v(H\beta)$, which is displayed in Fig. 8. Differences up to ± 150 km s^{-1} are measured, with uncertainties of typically 40 km s^{-1} (3σ). Strong positive values of observed $v([O III]) - v(H\beta)$ are located in the south-east half of our field of view, while strong negative values are found in the other half. These qualitatively follow the perturbations observed in the stellar kinematics (see Section 4.2).

We also show the velocity dispersion maps of Hβ and [O III] (right panels of Fig. 7). In both maps and if we exclude the nuclear regions, the regions of bright emission display a dispersion lower than their lower-surface-brightness surroundings. We checked that this was not a bias introduced by differences in signal-to-noise ratio between bright and weak regions.[2] The signal-to-noise ratio in our

---

[2] There is a systematic trend to obtain larger dispersion values as a result of the fit when the signal-to-noise ratio in a spectrum decreases.
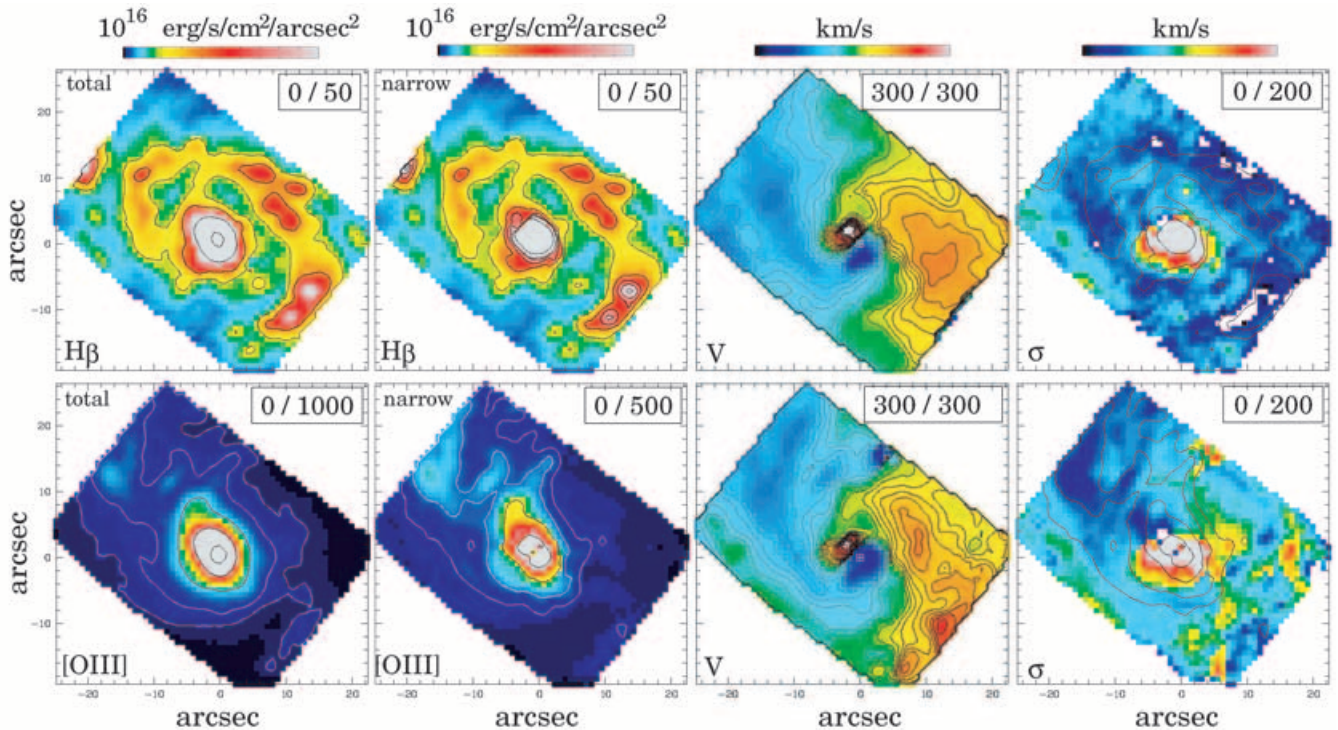
Figure 7. SAURON maps of the gas distribution and kinematics for NGC 1068. Top row (from left to right): distribution of the total and narrow components, and velocity and velocity dispersion for the Hβ narrow component. Bottom row: the same as the top row, but for the [O III] component. Boxes in the top right corner of each panel show the ranges covered by the colour bars.
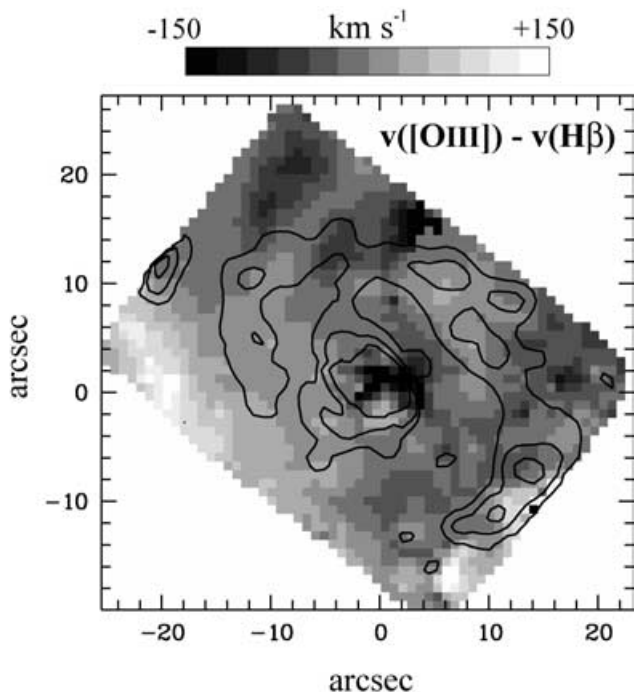

Figure 8. Reconstructed map of the difference between the centroid velocities of the [O III] and Hβ lines of the narrow component, with contours of the Hβ narrow-component map overimposed. Contours: 10, 20 and 40 erg s^{-1} cm^{-2}.

Hβ and [O III] observations is >20 over most of our field of view and our Monte Carlo simulations (see Section 2.5) show that, in this case, our relative uncertainties on the measured dispersion values are <10 per cent (3σ). We observe differences of the order of 0.5 Å for dispersion values of typically 2.5 Å and this trend is therefore real.

Lastly, we have built the map of the [O III]λ 5007/Hβ ratio (see Fig. 9). The range of variation of this ratio is extremely large with Hβ dominating in the arms (ratio below unity) and [O III] dominating in the ionization cone (ratio reaching values up to 13–14). The peak of a high [O III]/Hβ ratio around a PA of 30° corresponds to the northern ionization cone. Note that the presence of the well-defined peak suggests that, within the cone, the excitation of the gas decreases from its centre to its edges. However, this result must be taken with caution as the regions responsible for this peak are located at the very edge of our field of view.

There does not seem to be a systematic association between regions that exhibit large velocity differences between [O III] and Hβ (Fig. 8), and those with a high [O III]/Hβ ratio (Fig. 9). Outside a radius of 5 arcsec, we observe large velocity differences up to 100 km s^{-1} and rather normal [O III]/Hβ line ratios. This suggests that the observed kinematic disturbance is not directly linked with the AGN activity.

4.4 Comparison with the Hα and CO maps

The agreement between the SAURON Hβ flux and velocity maps with the corresponding Hα maps, as shown in Fig. 10, is remarkable considering the very different instrumental set-up and the fact that dust extinction is present (Bruhweiler et al. 2001). Apart from the central few arcseconds, where scattering effects are important and
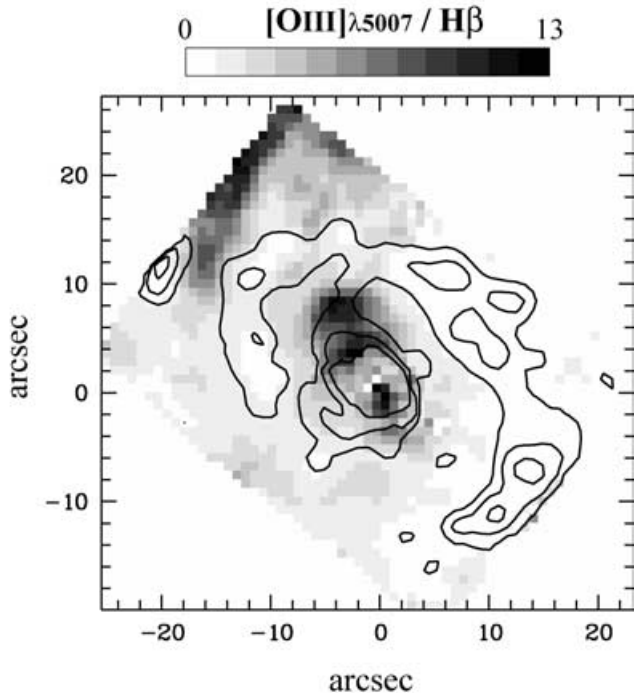
Figure 9. Reconstructed map of the [O III]λ 5007/Hβ ratio, with contours of the Hβ narrow-component map overimposed. Contours: 10, 20 and 40 erg s^{-1} cm^{-2}. A clipping has been applied to the map, setting pixels to a value of 0 where the relative accuracy of the ratio was worse than 20 per cent (only a few pixels south-west of the nucleus).

AGN related emission is present, extinction significantly affects Hβ (as probed by a ratio of Hα/Hβ well over 3; Bruhweiler et al. 2001) in the south-west part of the arm (south-west clump at a radius of about 14 arcsec; Bruhweiler et al. 2001). Both the Hα and Hβ velocity field exhibit a very strong spiral-like perturbation with the zero velocity curve displaying a very wavy shape. The Hα map is analysed further in Section 4.5.

A comparison between the maps of the ^{12}CO(1–0) line flux and the corresponding Hα emission is shown in Fig. 10. They both roughly follow the two-arm spiral structure with a diameter of about 40 arcsec (often mentioned as the circumnuclear ring). There are, however, some very significant differences, which we emphasize here. First, the Hα emission is much more asymmetric with respect to the centre with a brighter northern arm. Secondly, the CO spiral is clearly offset from the Hα arms: it is on the inner side of the south-west Hα clump, but seems to lie outside the Hα arm in the north-west. A similar comparison at higher spatial resolution using the *HST*/WFPC2 images (Bruhweiler et al. 2001) shows that the spiral arms seen in CO and Hα are in fact offset from each other (the northern and southern CO arms being outside and inside the corresponding Hα arms, respectively). This is commonly observed in spiral barred galaxies (Sheth et al. 2002). In the case of NGC 1068, the offset could be partly explained by the fact that most of the Hα emitting regions are associated with starbursting H II regions. Davies, Sugai & Ward (1998) thus showed that most of the young stars in the ring formed in compact clusters in a relatively recent short burst within the last 30 Myr, about 10 dynamical time-scales at the radius of the ring. However, extinction also plays a role here because A_V of ∼1–3 mag have been measured for these clusters (Davies et al. 1998). We therefore do not expect a perfect coincidence between the CO and Hα emission line gas (according to Davies et al. 1998, the ionization

cone cannot have a significant effect on the star formation). Because the near side of the disc is south of the nucleus, we cannot discard the possibility that we only clearly detect H II regions closer to the edge and in front of the molecular arms, which would explain the relative locations of the ionized and molecular arms. However, we do not have a good tracer of the currently ongoing star formation compared with the slightly older H II regions and it is therefore not possible to distinguish between the scenarios of dissociation of molecular gas due to hot stars, or segregation of CO and H II regions (as seen in the spiral arms of M83, M100, or M51, see e.g. Rand, Lord & Higdon 1999) due to a spiral density wave, or even some other unknown effect: observations of mid-infrared emission lines are required to test this.

4.5 Harmonic analysis of the Hα velocity field

Our SAURON Hβ and [O III] velocity fields, as well as the Hα one, exhibit complex kinematic features such as an S-shaped or wobbles in the zero velocity curve. We aim to extract the effect of the prominent NIR bar and that of the spiral arms from the velocity field of NGC 1068. Given that the Hα field covers a significantly larger area than the SAURON field (at the expense of a shorter spectral coverage), we will therefore apply our analysis method on the former. Assuming that circular motion is the dominant feature and that there is no strong warp in our field, we carry out an analysis based on the harmonic decomposition of the line-of-sight velocity V_{los} (Schoenmakers, Franx & de Zeeuw 1997; see also Franx, van Gorkom & de Zeeuw 1994). This formalism implies expanding the V_{los} field into harmonic series, where the first terms ($\cos\theta$ and $\sin\theta$) are the rotational and radial velocity components and the higher harmonic terms ($\cos m\theta$ and $\sin m\theta$) provide information about perturbations on the gravitational potential (Fathi 2004; Wong, Blitz & Bosma 2004). The first, second and third harmonic components, are sufficient for studying specific elements of the perturbations on the underlying potential. A perturbation of order m creates $m-1$ and $m+1$ line-of-sight velocity terms (e.g. Canzian 1993; Schoenmakers et al. 1997), i.e. third harmonic terms contain information about an $m = 2$ bar or a two-arm spiral perturbation.

To obtain the kinematic PA, the systemic velocity and the circular velocity contribution to the Hα V_{los} as a function of galactocentric radius, we apply a tilted-ring method similar to that by Begeman (1987). We first assume an inclination of 40°, then, for each galactocentric radius, we find the best-fitting PA and systemic velocity. These parameters did not show a significant variation throughout the field: the PA variation is found to be less than 10° and the V_{sys} varies by less than 20 km s^{-1}. Following the standard procedure, we then fix the PA and V_{sys} to the average values. This step yields PA = 87° and V_{sys} = 1140 km s^{-1}, which are consistent with the values mentioned in the rest of the present paper. Keeping these parameters fixed, we now fit the rotational component and derive the rotation curve presented in Fig. 11. Reconstruction of the circular velocity component and subtraction from the observed velocity field yields the residual non-circular velocities as presented in Fig. 11.

We explore the non-circular velocity components by fitting the residual map with the higher order harmonic terms up to and including order 3. The second harmonic terms are mainly consistent with zero. The first and third harmonic terms show a behaviour similar to that of an analytically derived logarithmic two-arm spiral perturbation (Wong et al. 2004). We therefore construct a library of velocity fields perturbed by two armed spirals with different spiral structure characteristics. The library of models includes a range of pitch angles, perturbation amplitudes and spiral arm sizes. We
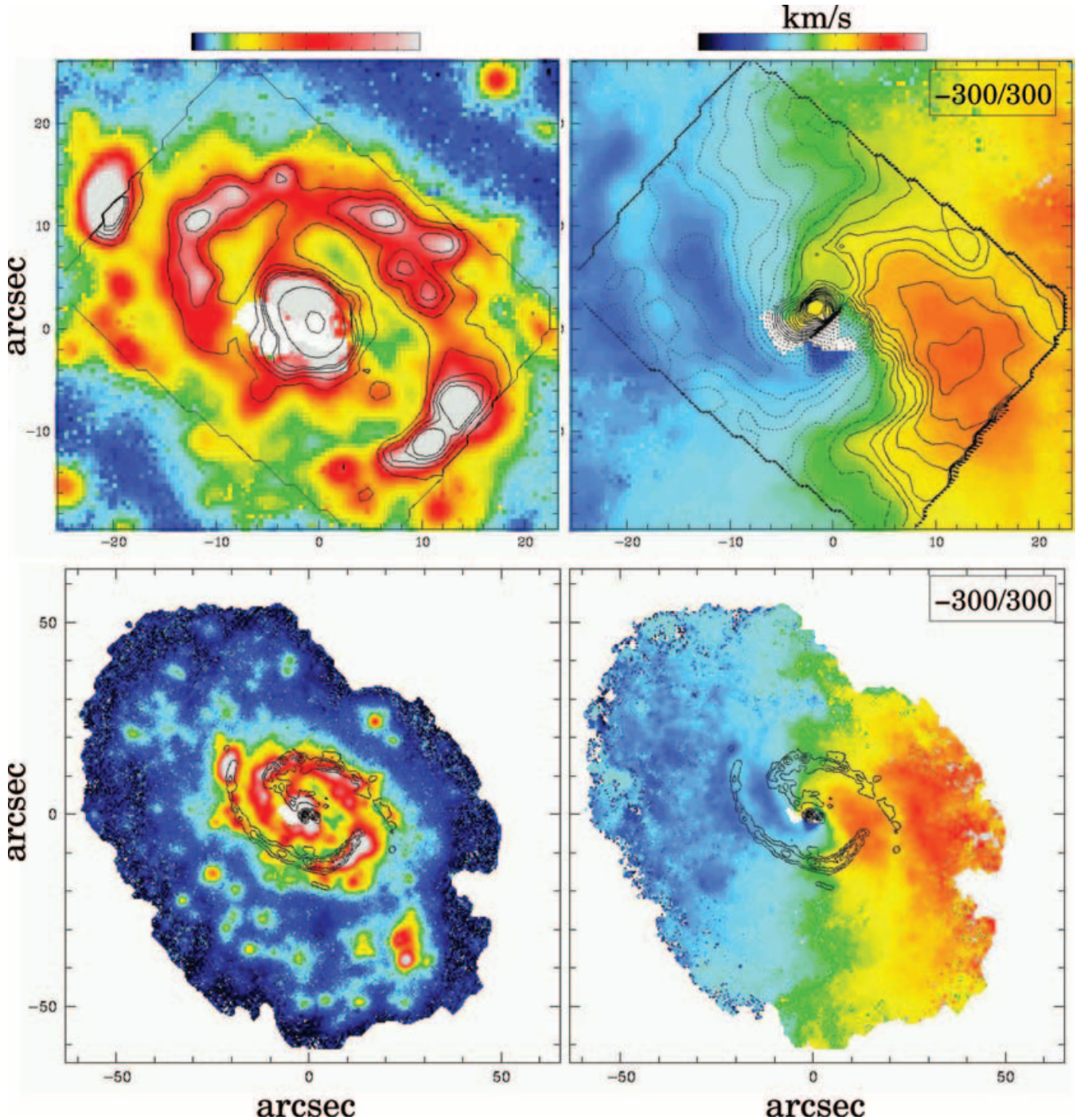
Figure 10. Top panels: comparison between the SAURON Hβ flux (contours, left panel) and velocity (contours, right panel) and the corresponding Hα maps obtained by Bland-Hawthorn et al. (1991) with HIFI. The velocity step used for the SAURON isovelocities is 25 km s^{-1}. Bottom panels: comparison of the Hα maps with the CO distribution (contours: Schinnerer et al. 2000). Boxes in the top right corner of each panel show the ranges covered by the colour bars.

compare the harmonic terms and non-circular velocity features with those of the models to find a model that best resembles the observed features. We find that the spiral model with a pattern speed $\Omega \sim 109 \pm 5$ km s^{-1} kpc^{-1}, a pitch angle of 15°, a spiral amplitude of 0.17 and with its CR at 31 arcsec provides the best fit to the observed Hα velocity field. However, in the region of the inner NIR bar, there is significant disagreement between this model and the observed maps, the spiral model alone being obviously inadequate for describing the observed features.

4.6 Application of the Tremaine–Weinberg method

RW04 recently argued for the presence of two different pattern speeds for the NIR inner bar and the spiral arms that surround it in NGC 1068. They quote a value of $\Omega_p \sim 135 \pm 42$ km s^{-1} kpc^{-1} for the inner bar and a lower value of $\Omega_p^S \sim 72 \pm 4$ km s^{-1} kpc^{-1} for the outer spiral arms via the Tremaine–Weinberg method (Tremaine & Weinberg 1984) applied to the CO molecular line data. This estimate for the pattern speed of the inner bar should be taken as a lower
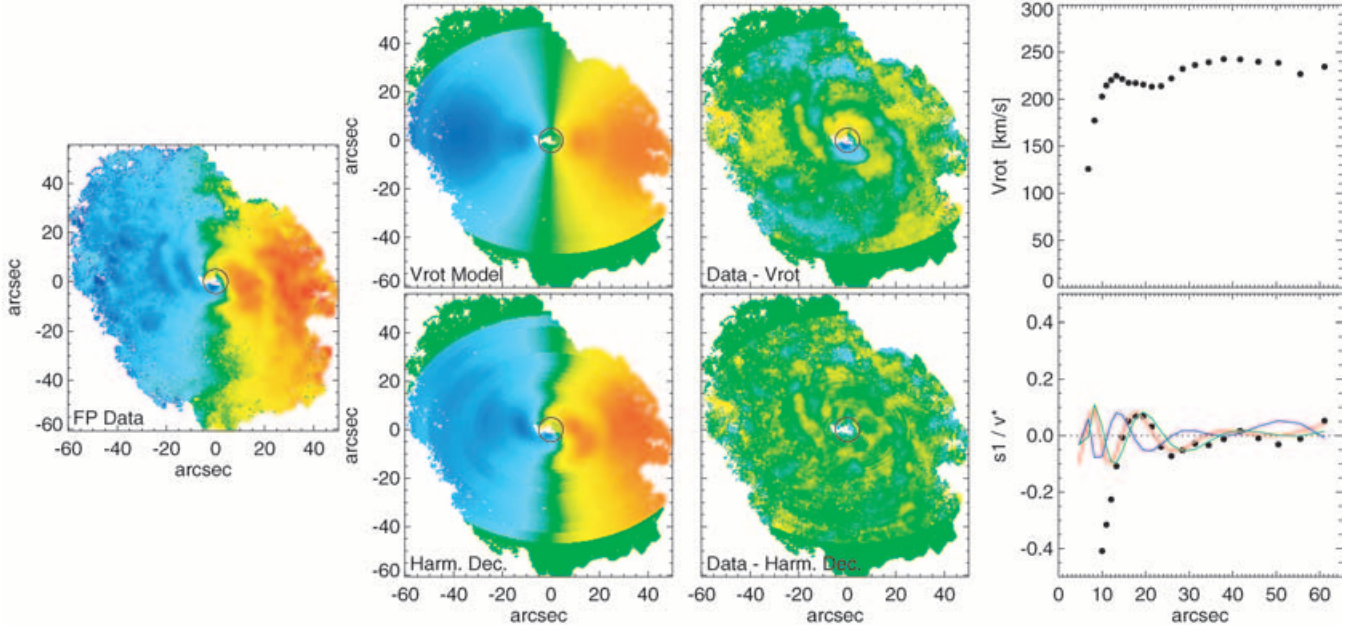
Figure 11. Left panel: observed Hα velocity field. Top row, from left to right: best-fitting circular velocity component alone, corresponding residual map (Data − $V_{\rm rot}$ model) and the derived rotation curve assuming an inclination of 40°, PA = 87° and $V_{\rm sys}$ = 1140 km s^{-1}. Bottom row, from left to right: harmonic reconstruction including the rotational velocity component, corresponding residual map (Data − Harmonic Decomposition Fit) and the derived radial velocity component normalized with $v^* = V_{\rm rot} \sin(i)$ as a function of galactocentric radius. The solid curves in the bottom right panel show the radial velocity component according to the analytic spiral model as described in Section 4.5. The best-matching spiral model with CR at 31 arcsec corresponding to the spiral pattern $\Omega_{\rm p} = 109 \pm 5$ km s^{-1} kpc^{-1} is shown in red. Radial velocities for spirals with pattern speeds of 99 and 119 km s^{-1} kpc^{-1} are shown in green and blue colours, respectively.

limit, considering the presence of a second outer tumbling component. The validity of using this technique on a gaseous component was tested by RW04 with *N*-body + SPH simulations. A similar test was also recently performed by Hernandez et al. (2005) who emphasized the need to avoid regions of shocks. We attempted to estimate the pattern speed of the spiral and bar structures in NGC 1068 via the same technique but on the large-scale Hα maps of Bland-Hawthorn et al. (1991): these clearly have a higher resolution (and thus provide more apertures) but a more clumpy distribution than the CO maps. We confirm the trend found by RW04 and clearly detect two different patterns, for points inside or outside 20 arcsec. The scatter of the ⟨*V*⟩ versus ⟨*X*⟩ diagram (see Fig. 12) is small for the outer region with a well-defined slope of 80 ± 2 km s^{-1} kpc^{-1} for a PA of 90°, only slightly higher than the value found by RW04. However, this slope strongly varies from 56 to 104 km s^{-1} kpc^{-1} when we assume a PA varying from 84° to 95°, a dependency already emphasized by RW04 and Debattista (2003; see also Debattista & Williams 2004). The pattern speed of the inner region is rather badly constrained by our data, an expected result considering the presence of star-forming regions and the influence of the ionization cone. Using the odd parts of ⟨*V*⟩ and ⟨*X*⟩ data points to minimize the scatter (Tremaine & Weinberg 1984), we find a lower limit value of 133 ± 12 km s^{-1} kpc^{-1} for PA = 90° (consistent with the value of RW04) and from 93 up to 178 km s^{-1} kpc^{-1} for PAs again varying from 84° to 95°.

5 *N*-BODY MODELLING

We now turn to the dynamical modelling of the central region of NGC 1068 using *N*-body and SPH simulations. This will be compared in Section 5.3 with the SAURON maps of the gas and stellar kinematics, as well as with the available H I, Hα and CO data (see Section 3).
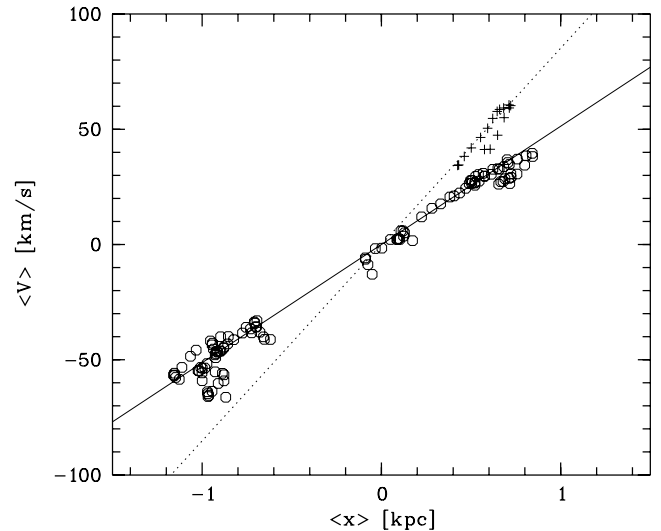

Figure 12. Tremaine–Weinberg method applied on the Hα Fabry–Perot maps of Bland-Hawthorn et al. (1991). The averaged, density-weighted velocity ⟨*V*⟩ is plotted against the averaged, density-weighted coordinates ⟨*X*⟩, along slits parallel to the line of nodes assuming PA = 90°. The best-fitting slopes for the outer points (open symbols, *R* > 20 arcsec) and inner points (crosses, 8 arcsec < *R* < 15 arcsec) are shown as a solid and dotted line, respectively.

5.1 Methods

We used PMSPH, the *N*-body code initially developed in Geneva (Pfenniger & Friedli 1993). The gravitational forces are computed with a particle-mesh method using a 3D polar grid with $(N_R, N_\phi, N_Z) = (40, 32, 64)$ active cells. The hydrodynamics

equations are solved using the SPH technique (Friedli & Benz 1993). Because the radial spacing of the cells is logarithmic, the cell size increases from 15 pc at the centre to 383 pc at a radius of 2 kpc. 20 cells (i.e. half the number of radial cells) are used to described the region enclosed by SAURON field. The total grid has a radius of 100 kpc. All runs were performed using a total of 978 572 particles for the stellar part and 50 000 for the gaseous one. The initial conditions (positions, velocities, velocity dispersions) were built from a Monte Carlo realization of a five-component axisymmetric model, as described below, and the total running times for each simulation varied from 500 to 2000 Myr.

5.2 Mass model and initial conditions

We constrained the initial axisymmetric mass model of NGC 1068 by using the available photometry and velocity curve as constraints. We performed this in two steps. We first constrained the projected luminosity distribution of the galaxy by combining a high-resolution NIR *K*-band image (see Section 3) with the 2MASS *K*-band image, the DSS *I*-band image and a deep wide-field *B*-band image (see Section 3.1). The NIR images clearly reveal the bar within the central 20 arcsec, and the optical images allowed us to estimate the contribution of the outer oval and disc structures (see Section 3). We assumed the presence of a central spherical bulge and fitted a projected Plummer sphere to the high-resolution NIR *K*-band image. This component was subtracted from all images, which were then simply deprojected by assuming an inclination angle of $i = 40°$ and a two-dimensional distribution: this corresponds to a spatial scale factor of $\sim$1.3 perpendicularly to the line of nodes. The deprojected images were found to be reasonably approximated by the sum of four individual Miyamoto–Nagai components, each of them probing a different scale (see Table 1).

We normalize each component, i.e. the four Miyamoto–Nagai, the Plummer sphere and one additional Miyamoto–Nagai component for the gas, so that the resulting circular velocity curve fits the observed H I velocity profile. This requires the overall mass-to-light ratio to increase by a factor of 10 between the central part and the outer most point of the H I curve ($R = 180$ arcsec). Because we know that the simulation will rapidly depart from its initial conditions, this procedure is only meant to produce a three-dimensional mass distribution, which reproduces the radial mass gradient, the central bulge concentration and the large-scale velocity curve reasonably well. We consider the contribution of a presumed central black hole to be

Table 1. Parameters of the initial conditions used in the *N*-body + SPH simulations. M–N and P stand for Miyamoto–Nagai and Plummer components, respectively.

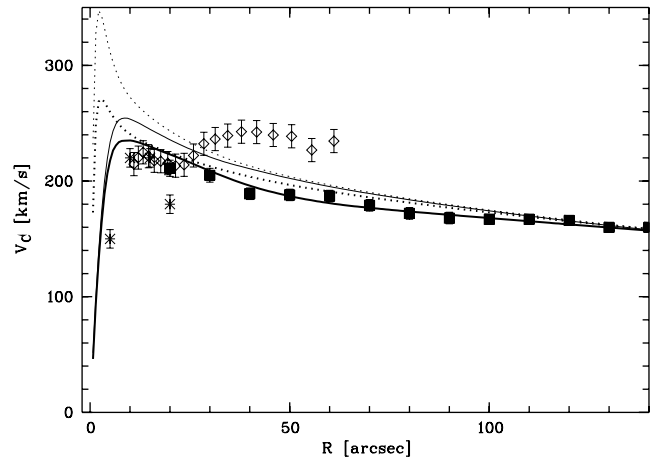| Component	Type	No.	Mass (10^9M$_\odot$)	*a* (kpc)	*b* (kpc)
Model A					
Stars	M–N	1	4.4	0.255	0.035
Stars	M–N	2	18.7	1.0	0.1
Stars	M–N	3	46.2	5.0	0.2
Stars	P	4	3.3	–	0.1
Gas	M–N	–	3.4	6.0	0.2
Model B					
Stars	M–N	1	2.4	0.155	0.035
Stars	M–N	2	18.7	0.8	0.2
Stars	M–N	3	46.2	4.6	0.4
Stars	P	4	3.3	–	0.1
Gas	M–N	–	3.4	6.0	0.2

Figure 13. Circular velocity profiles of the *N*-body + SPH simulations at $t = 0$ (dotted lines) and at the end of the runs (solid lines) compared with observed velocity profiles. $t = 850$ Myr for model A (thick lines) and $t = 1440$ Myr for model B (thin lines). Symbols show the deprojected H I (filled squares), Hα (diamonds; from this paper) and CO (stars) velocity profiles (assuming an inclination of $i = 40°$).

part of the Plummer sphere. The initial radial profiles of the circular velocity are presented in Fig. 13.

We performed a number of runs (36), where we mainly varied the concentration of the different components, keeping the total mass (including the gas) roughly constant (see below). We chose to ignore the observed Hα velocity profile as a constraint for the initial conditions of our models, as it exhibits strong non-circular motions (e.g. see Section 4.5). We present only two models here (A and B), as they are typical of the runs performed and their initial circular velocity profiles roughly bracket the observed H I profile of NGC 1068 (Fig. 13). Both models have initial conditions that are consistent with a deprojected axisymmetric version of the available *K*-band images. This is illustrated for model B in Fig. 14, in which we show the projected mass profiles compared to 2MASS *K*-band surface brightness profiles. The corresponding gravitational potential and density distributions in the meridional plan are presented in the same figure.

5.3 Models A and B

A bar starts forming around 300 Myr, but becomes prominent only after 900 Myr for model A. The bar forms much later on in model B, this being mainly due to its significantly higher mass concentration. The overall evolution of model B is much slower for the same reason. In simulations with even higher mass concentrations, the disc was found to be stable against the formation of a bar. It is important to note that the central Plummer sphere has a characteristic scale (100 pc), 6 times the central resolution grid point (15 pc). After the bar formation, the gas wraps around in a low-contrast multi-arm spiral structure for a few 100 Myr. The gas then reacts quickly to the formation of the $m = 2$ perturbation and is radially redistributed. Part of the gaseous component flows towards the central 500 pc, exhibiting a time varying structure. We derived a snapshot of both simulations after the bar is well formed, the time of each snapshot being chosen ($t = 850$ for model A and 1440 Myr for model B) such as to resemble the overall structure of the gaseous component in NGC 1068. We optimized the viewing angles for the bar to lie at a PA of 44°.5, as in NGC 1068, and the zero velocity curve to be
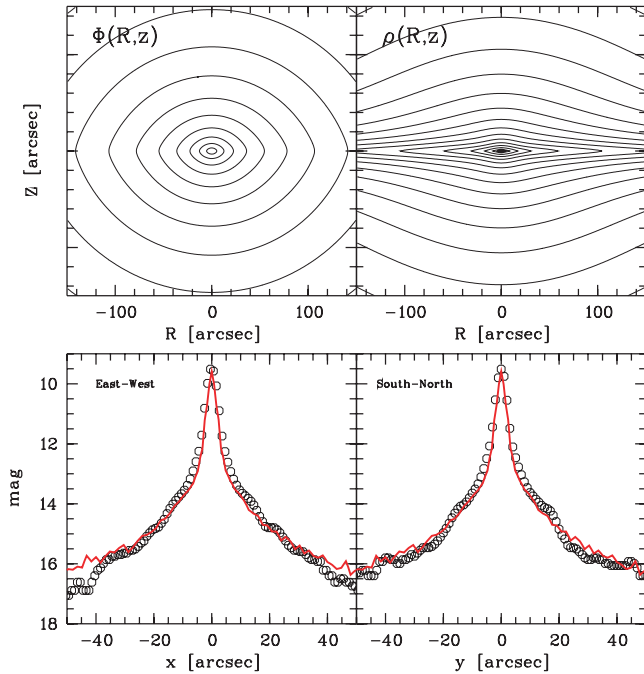
Figure 14. Initial conditions for model B. Top panels: potential (left) and density (right) isocontours in the meridional plane (R, z). Contour steps are 0.1 and 0.5 in log, respectively. Bottom panels: (projected) surface brightness profiles along the east–west (left) and south–north (right) direction extracted from the K-band 2MASS images (open circles) and model B after projection using an inclination of $40°$ (solid lines).

as close as possible to the observed one. This requires (for a fixed inclination of $40°$) that the line of nodes is at a PA of $\sim 83°$ and $84°$ for models A and B, respectively. We have tested the dependence of this value on the time of the snapshot as well as on varying initial conditions: the resulting PA of the line of nodes varies then between $80°$ and $90°$.

5.4 Comparison with the observed stellar kinematics

The simulations performed for this study are intended as a proof of concept and not as perfect fits to the data. The kinematics are luminosity weighted and we did not include star formation or dust extinction in our simulations, although it is clear that young stars and dust significantly affect the surface brightness at the wavelengths of the SAURON observations. Furthermore, the bars formed in these simulations do not perfectly match the well-known NIR bar and we could not reproduce the large-scale (north–south) oval in the photometry (the suggested signature of a large-scale bar).

Model A fits the H I inner velocity profile better than model B (both models having similar circular velocities outside 100 arcsec), but significantly fails to reproduce the first two stellar velocity moments (velocity and velocity dispersion), with values significantly below the observed data. We will therefore focus on the results from model B in the rest of the paper. The bar in model B has a pattern speed of ~ 100 km s^{-1} kpc^{-1}, which leads to radii for the inner inner and outer inner Lindblad resonances (IILR, OILR), the 4:1 ultraharmonic resonance (UHR), the CR and the OLR of 5.2, 10.5, 22.6, 32.2 and 50.2 arcsec, respectively (0.36, 0.73, 1.58, 2.25 and 3.50 kpc, respectively). This implies that the NIR bar ends well inside its CR, closer to its UHR.

A comparison of the stellar kinematics of model B within the SAURON field of view is presented in Fig. 15: it looks qualitatively

similar to the observed SAURON maps. The twist in the stellar velocity field is less pronounced in the model, which nevertheless shows the clear signature of non-axisymmetry. A more quantitative comparison is shown in Fig. 16, where a few cuts at PA $= 90°$ of the stellar velocity fields are presented against the SAURON data. The overall agreement is quite good, with the exception of the outer parts of the central profile in which there is a discrepancy of about 20 km s^{-1}: this is where we detected perturbations in the stellar kinematics (Section 4.2). As mentioned already, they follow the velocity differences between the Hβ and [O III] emission lines (Section 4.3). The discrepancy between the model and observed stellar kinematics therefore mostly reflects the presence of streaming motions within the outer spiral arms, where star formation is ongoing. Model B additionally reproduces the morphology of the observed h_3 field, with the zero h_3 curve almost following the major axis of the bar, as in the SAURON map. There is only a slight central depression in the h_4 map of model B, less pronounced than in the data. The model does also not reproduce the ring-like enhancement of h_4 observed both in the SAURON and long-slit data.

We can now compare the obtained stellar kinematics with the more extended long-slit kinematics obtained from the data of Sh+03: a comparison is presented in Fig. 17. The agreement is again very reasonable, including the higher order Gauss–Hermite moments. However, the kinematic profiles of the simulations do not exhibit the characteristic dispersion peaks at a radius of ~ 22 arcsec on either side of the centre along the major axis. These peaks correspond to a transition region at the end of the bar, where the slope of the velocity gradient also changes, and are close to the UHR in model B. The simulations also lack the central plateau or depression in the dispersion profile observed in the central 5 arcsec of NGC 1068.

6 DISCUSSION

6.1 The location of resonances

Both the molecular and ionized gas kinematics exhibit strong departures from circular motion (see e.g. Fig. 11) and the presence of the NIR bar in the inner 1.5 kpc is undisputable. The Hα (Fig. 10) and CO velocity fields (S+00) provide us with an important clue regarding the kinematics of the spiral arms: the isovelocities clearly bend outwards, which implies an inward streaming motion (e.g. see the spiral arm velocity contours at about 10 arcsec south, 5 arcsec west). A similar argument was initially emphasized by Yuan & Kuo (1998), although they reached the opposite conclusion as they relied at the time on the CO data of Helfer & Blitz (1995), which lacked spatial resolution and seemed to show an inward bending.[3] The inward streaming therefore requires the gas to be located inside the CR or outside the OLR of the corresponding density wave, a conclusion also reached by S+00 and RW04 (and opposite to the one of Yuan & Kuo 1998, but see above).

The presence of a large-scale tumbling component with a radius of about 9 kpc is debatable, although a very significant elongation is clearly observed in the photometry at a PA near the minor axis, inconsistent with an axisymmetric outer disc. S+00 first estimated the pattern speed of the outer oval[4] to be $\Omega_p \sim 35$ km s^{-1} kpc^{-1}. Assuming the ILR of the primary bar corresponds to the CR of

---

[3] Yuan & Kuo (1998) also noted that they 'would not be surprised' to get a different result when a more reliable rotation curve becomes available.

[4] S+00 quote a value of $\Omega_p = 20$ km s^{-1} kpc^{-1} in their paper, although, as mentioned by RW04, they actually used a value of 35 km s^{-1} kpc^{-1}.
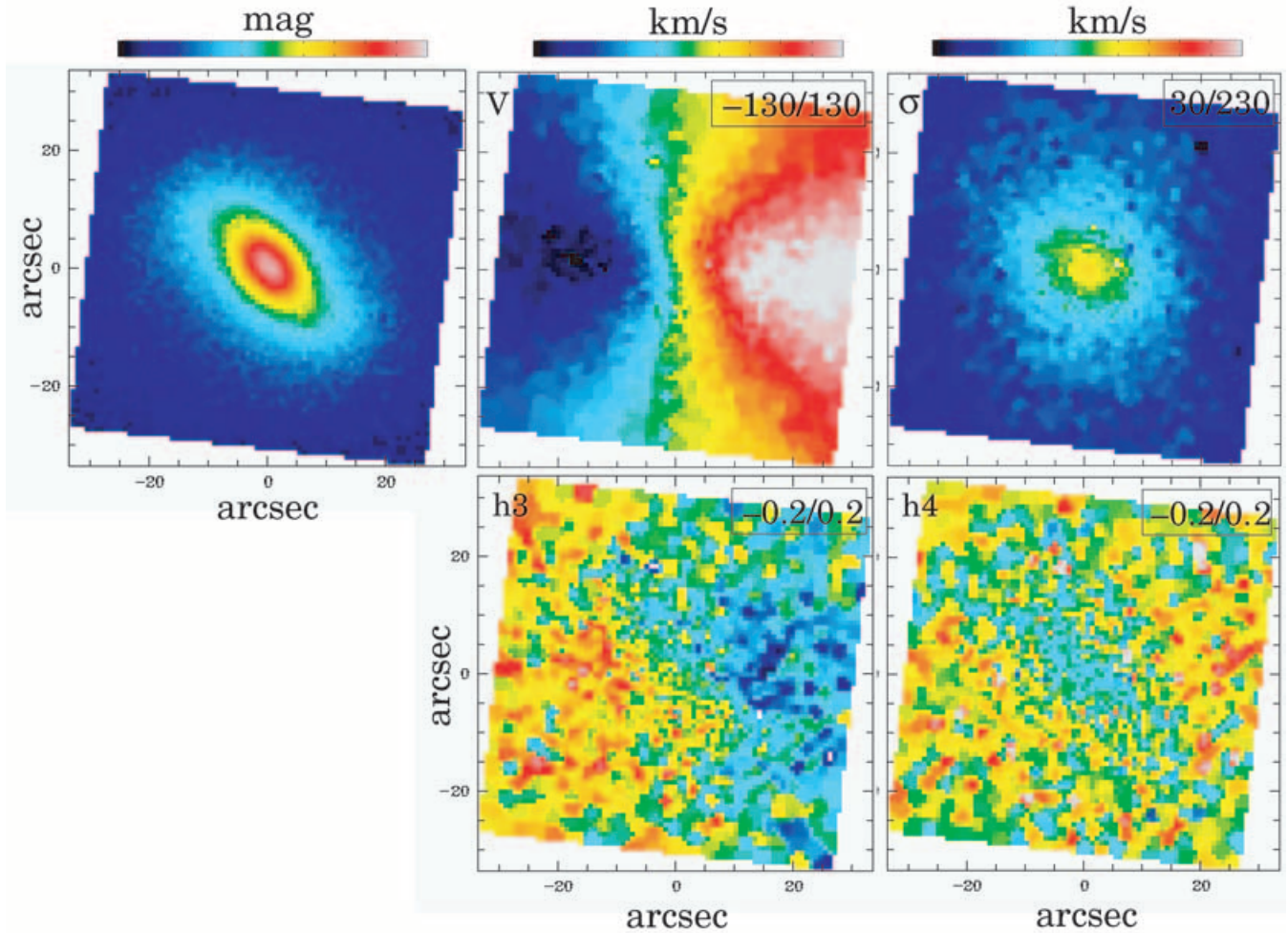
Figure 15. Luminosity distribution (top left panel, assuming a constant mass-to-light ratio) and observed stellar kinematics from the model B at $t = 1440$ Myr (using an inclination of $i = 40°$). The panels correspond to the ones in Fig. 5. Boxes in the top right corner of the panels show the ranges covered by the colour bars.

the inner (secondary) bar, they determine its pattern speed to be $\Omega_s \sim 140$ km s^{-1} kpc^{-1}. This would imply that the gaseous spiral arms lie between the CR and ILR of the primary bar. However, these arms would lie outside the CR of the secondary bar and the assumed value for Ω_s would make the NIR bar extend as far as its CR. Recent simulations of double bars (Rautiainen, Salo & Laurikainen 2002) seem indeed to favour CR/ILR coupling (but see Moellenhoff, Matthias & Gerhard 1995), but with short secondary bars, ending inside the 4:1 UHR. This requires the pattern speeds for both the primary and secondary bar to be lower.

Assuming the PA of the line of nodes is between $84°$ and $90°$ (Section 5.4), a lower limit for the pattern speed for the inner bar is estimated to be between 93 and 133 km s^{-1} kpc^{-1} (Tremaine–Weinberg method on the Hα data, see Section 4.6), while the bar that forms in model B has a pattern speed of 100 km s^{-1} kpc^{-1} (Section 5.4). These values would be consistent with the inner bar ending inside its UHR as discussed above. If we believe the outer oval corresponds to a third tumbling structure (S+00), a CR/ILR coupling between the two bars would then imply a primary bar with $\Omega_p \sim 25$ km s^{-1} kpc^{-1}, lower than but still consistent with the value advocated by S+00.

As mentioned above, the N-body simulations conducted in this paper lead to a PA for the lines of nodes in the range $84°$–$90°$ with a preferred value of $84°$. This is consistent with the photometric PA of the outer disc and with the output of the tilted-ring gas modelling (Section 4.5). It is not consistent with the H I kinematic axis determined by Brinks et al. (1997). However, Brinks et al. noticed a gradual change in the PA of the H I kinematic major axis, which they interpreted as the sign of a mild warping. The H I map exhibits a weak spiral arm or ring-like structure in the radius range 130–180 arcsec, the density decreasing then inwards (down to the inner H I ring present between 30 and 80 arcsec; Brinks et al. 1997). If the outer oval is, as mentioned above, a weak bar tumbling at 25 km s^{-1} kpc^{-1}, its OLR would be located at a radius of 140 arcsec (10 kpc), within the outer H I structure. At the OLR, we expect periodic orbits to be elongated perpendicularly to the major axis of the bar. The observed radial variation in the H I kinematics could therefore be partly explained by the resulting non-circular motions. However, this should be confirmed by a detailed kinematic H I study in the outer region of NGC 1068.

We finally turn to the derivation of the pattern speed associated with the outer spiral arms. Our estimate using the Tremaine–Weinberg technique is between 56 and 80 km s^{-1} kpc^{-1} (for PAs between $84°$ and $90°$), consistent with the values given by RW04. However, this is significantly lower than the estimate obtained via the harmonic decomposition (Section 4.5), which provides a value
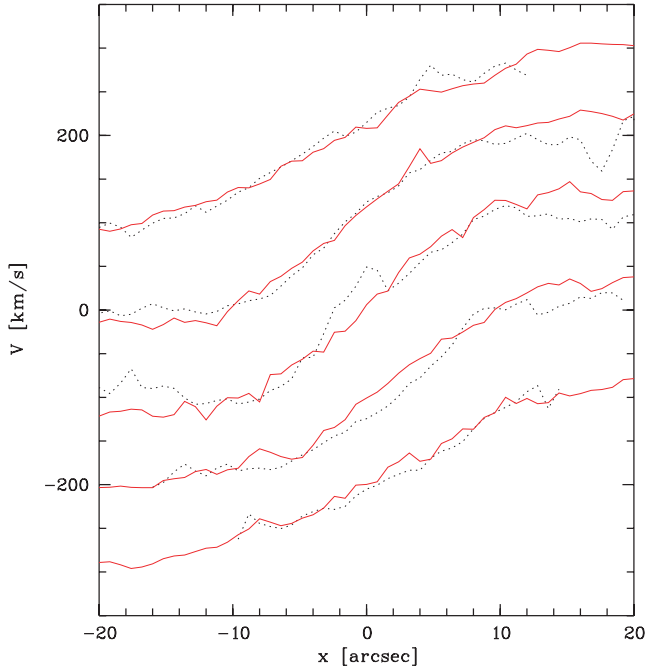
Figure 16. Comparison between stellar kinematic profiles extracted from the two-dimensional SAURON velocity field (solid lines) and from model B at $t = 1440$ Myr (dashed lines). Four cuts along PA = 90° are shown, with offsets, from top to bottom, of 10, 5, 0, -5 and -10 arcsec, respectively.
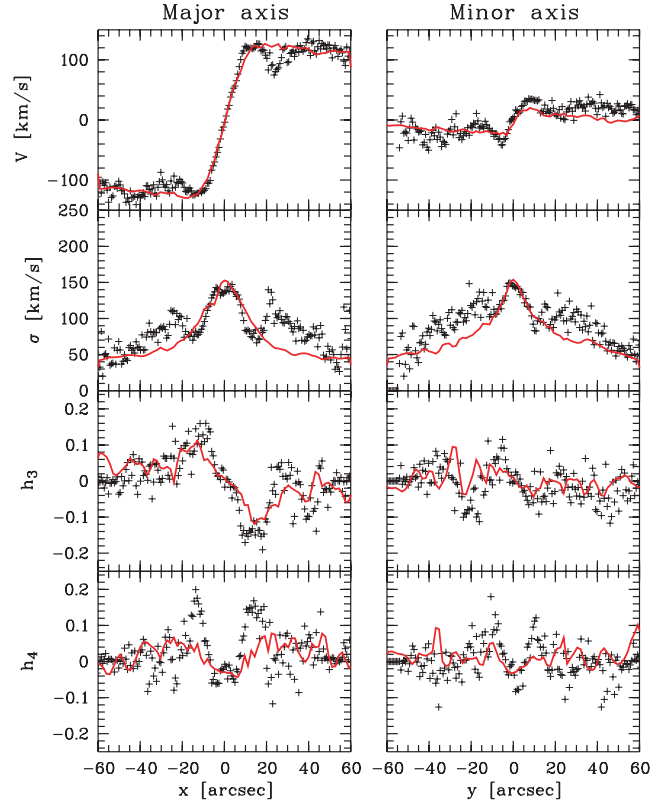

Figure 17. Comparison between stellar kinematic profiles extracted from Sh+03 (crosses) and from model B at $t = 1440$ Myr (solid lines). From top to bottom: mean velocity, velocity dispersion, h_3 and h_4. The model kinematics have been averaged over a slit width of 3 arcsec.

close to the estimate of the pattern speed of the NIR bar. If the outer spiral and the inner bar share the same pattern speed, it would hint at the bar being the main driver. However, the outer spiral and the inner bar having different pattern speeds would not be unexpected as modes can couple non-linearly (Masset & Tagger 1997). Such a process is witnessed in some simulations of double bars (see e.g. Rautiainen et al. 2002) which exhibit up to four different $m = 2$ modes. However, it would not be wise, considering the large uncertainties in the determination of the tumbling frequencies, to speculate further if non-linear coupling of modes is present in NGC 1068. The pattern speed of the outer spiral is in all cases much higher than the one of the presumed large-scale bar.

6.2 Signatures of the bar

Bureau & Athanassoula (2005) drew attention to a number of the stellar kinematics signatures of a bar using pure *N*-body simulations: a double hump velocity profile, correlated stellar *V* and h_3 profiles within the bar, secondary peaks for the dispersion σ near the end of the bar, a flat central minimum in the h_4 profile followed by a significant rise and a decline at larger radii. However, these features were obtained for rather high inclination ($i > 75°$) and for a galaxy with a very prominent outer stellar ring. There are secondary peaks in the observed dispersion profiles of NGC 1068 at a radius of 22 arcsec for a PA of 80° (see e.g. Fig. 17) and a flat minimum in h_4 which corresponds to the flat central part in σ (within a radius of 5 arcsec). However, although there is a local minimum in *V* corresponding to the secondary σ maxima, the double hump nature of the velocity profile is not very pronounced: the outer stellar velocity curve is nearly flat with a level comparable to the inner maximum of ~ 120 km s^{-1} at radii between 10 and 15 arcsec. We furthermore observe h_3 profiles that are clearly anticorrelated with *V* within the extent of the bar: this means that we detect a tail of low-velocity

stars superimposed on the rapidly rotating ones along the line of nodes.

The high-resolution *K*-band image of NGC 1068 obtained by Peletier et al. (1999) shows the inner bar with rather pinched ends at a radius of ~ 16 arcsec. These can be interpreted as the tips of the x_1 orbits sustaining the bar. There is a clear plateau in the surface brightness profile around that radius, which is also the witness of a radial (and possible vertical) redistribution of the stellar component (Combes et al. 1990). The fact that we do not reproduce the higher stellar dispersion (and lower stellar velocity) around a radius of 22 arcsec (PA = 80°, Fig. 17) with our simulations may be due to the lack of star formation in our models. This region in NGC 1068 is the site of intense star formation and corresponds to the UHR of model B: stars often form near the UHR (Schwarz 1984; Buta & Combes 1996), and gathering new stars with orbits at the UHR (4:1 resonance) may be the cause of an increase in the stellar velocity dispersion.

6.3 Driving gas towards the central 300 pc

Star formation could also be the cause of the discrepancy between the rather flat (or depressed) central dispersion profile of NGC 1068 and that of model B. The inner bar is able to drive gas inwards, as illustrated by some numerical simulations of double barred galaxies (see Model III of Rautiainen et al. 2002) although this is certainly not a generic result for double bars (e.g. Maciejewski et al. 2002). If we assume that the NIR bar ends well inside its CR, it then implies the presence of an ILR around 5 arcsec. This would roughly coincide

with the extent of the stellar velocity decoupling and σ drop, and it would support the generic scenario outlined by Emsellem et al. (2001) and Wozniak et al. (2003): the inner NIR bar has driven gas within its ILR, thus forming a relatively cold stellar system within the central few hundred parsecs.

We are indeed witnessing radial gas inflow in the central kpc in our numerical simulations. The inflow rate in model B ranges from 10^{-2} to a few $M_\odot \, yr^{-1}$ within the region of the bar, with an average of about $5 \times 10^{-2} \, M_\odot \, yr^{-1}$. This gaseous mass inflow increases significantly as the bar gets stronger. The net mass increase driven by the bar 300 Myr after its formation is $\sim 5 \times 10^7 \, M_\odot$ inside 5 arcsec (350 pc), which represents about 1 per cent of the total enclosed mass. All these values should be taken as upper limits as, for example, the simulations do not include star formation. In order to make the link with still smaller scales, high-resolution two-dimensional mapping of the stellar kinematics and populations in the inner few arcseconds would be required: a considerable challenge given the active and disturbed nuclear environment of NGC 1068.

7 CONCLUSIONS

We have successfully obtained stellar and gaseous kinematics for NGC 1068 over a large two-dimensional field covering the entire NIR inner (secondary) bar. Although our spectra exhibit numerous emission and absorption features, we have been able to disentangle the two components and derive the kinematics independently. Our SAURON data reveal a regular stellar velocity field that rules out an offset stellar system as claimed by García-Lorenzo et al. (1997). The SAURON two-dimensional stellar kinematics exhibit the signatures of the presence of the inner bar: a twist in the velocity field and an h_3 field elongated along the bar. These features are also retrieved in a qualitative comparison with N-body + SPH simulations.

We detect a kinematic decoupling of the central 350 pc (5 arcsec) in a reanalysis of previously published long-slit data (Sh+03). We first observe a flattening of the h_3 profile indicating a change of orbital structure within this region. We then reveal a flattening or a potential drop in the central part of the stellar velocity dispersion profile. The kinematics of the ionized Hβ and [O III] gas both show strong inward streaming motions. Differences up to 100 km s^{-1} are observed in the ionized gas kinematics inferred from the Hβ and [O III] lines. The CO and Hα distributions are not coincident, a difference which can be explained by the effect of the ongoing star formation and dust extinction.

We confirm the presence of two different pattern speeds for the region inside and outside of the inner bar (RW04), applying the Tremaine–Weinberg method to the Hα velocity field. However, the pattern speed of the inner bar is only weakly constrained. Note that the outer oval could correspond to a third tumbling structure, as mentioned by S+00.

We then performed numerical simulations with initial axisymmetric conditions approximating the photometry of NGC 1068. We focus on one model that has a gravitational potential consistent with the H I velocity profile and in which a bar forms. After projection with the relevant viewing angles, the resulting stellar kinematics successfully reproduce a number of properties observed in the SAURON and long-slit kinematics, including the h_3 and h_4 profiles. However, there are some discrepancies between the model and the observations, which could be partly explained by the exclusion of star formation and the lack of a primary large-scale bar in our simulations.

Finally, we briefly discuss the possibility of gas fuelling within the inner bar. The numerical simulations suggest that the inner bar

could drive a significant amount of gas down to a scale of $\sim$300 pc (its ILR). This would be consistent with the interpretation of the σ drop (Emsellem et al. 2001) in NGC 1068 being the result of central gas accretion followed by an episode of star formation (Emsellem et al. 2001; Wozniak et al. 2003). However, we should wait for a detailed view of the stellar kinematics and populations within the inner 300 pc to conclude on this issue: for example, with an integral-field spectrograph in the NIR, such as the Single Far Object Near-IR Investigation (SINFONI) at the Very Large Telescope (VLT). It would also be important to examine a sample of carefully chosen galaxies, as to allow a statistical analysis and to assess the relative contributions of the various physical mechanisms at play.

REFERENCES

Arribas S., Mediavilla E., García-Lorenzo B., 1996, ApJ, 463, 509
Arribas S., Mediavilla E., García-Lorenzo B., del Burgo C., 1997, ApJ, 490, 227
Arribas S., Mediavilla E., del Burgo C., García-Lorenzo B., 1999, ApJ, 511, 680
Athanassoula E., 1992, MNRAS, 259, 345
Bacon R. et al., 2001, MNRAS, 326, 23
Begeman K. G., 1987, PhD thesis, Univ. Groningen

Bland-Hawthorn J., Sokolowski J., Cecil G., 1991, ApJ, 375, 78

Bland-Hawthorn J., Gallimore J. F., Tacconi L. J., Brinks E., Baum S. A., Antonucci R. R. J., Cecil G. N., 1997, Ap&SS, 248, 9

Brinks E., Skillman E. D., Terlevich R. J., Terlevich E., 1997, Ap&SS, 248, 23

Bruhweiler F. C., Miskey C. L., Smith A. M., Landsman W., Malumuth E., 2001, ApJ, 546, 866

Bureau M., Athanassoula E., 2005, ApJ, 626, 159

Buta R., Combes F., 1996, Fundam. Cosmic Phys., 17, 95

Canalizo G., Stockton A., 2001, ApJ, 555, 719

Canzian B., 1993, ApJ, 414, 487

Capetti A., Macchetto F. D., Lattanzi M. G. 1997, ApJ, 476, L67

Cappellari M., Emsellem E., 2004, PASP, 116, 138

Cecil G., Bland J., Tully R. B., 1990, ApJ, 355, 70

Cecil G., Dopita M. A., Groves B., Wilson A. S., Ferruit P., Pécontal E., Binette L., 2002, ApJ, 568, 627

Cheng K. P., Collins N., Angione R., Talbert F., Hintzen P., Smith E. P., Stecher T., The UIT Team, 1997, UITVi, Vol. U, UV/visible Sky Gallery (CDROM)

Combes F., 2003, in Collin S., Combes F., Shlosman I., eds, ASP Conf. Ser. Vol. 290, Active Galactic Nuclei: from Central Engine to Host Galaxy. Astron. Soc. Pac., San Francisco, p. 411

Combes F., Debbasch F., Friedli D., Pfenniger D., 1990, A&A, 233, 82

Chung A., Bureau M., 2004, AJ, 127, 3192

Davies R. I., Sugai H., Ward M. J., 1998, MNRAS, 300, 388

Debattista V. P., 2003, MNRAS, 342, 1194

Debattista V. P., Williams T. B., 2004, ApJ, 605, 714

Dehnen W., Bland-Hawthorn J., Quirrenbach A., Cecil G. N., 1997, Ap&SS, 248, 33

Emsellem E., Greusard D., Combes F., Friedli D., Leon S., Pécontal E., Wozniak H., 2001, A&A, 368, 52

Emsellem E. et al., 2004, MNRAS, 352, 721

Fathi K., 2004, PhD thesis, Univ. Groningen

Ferruit P., Binette L., Sutherland R. S., Pécontal E., 1997, A&A, 322, 73

Ferruit P., Mundell C. G., Nagar N. M., Emsellem E., Pécontal E., Wilson A. S., Schinnerer E., 2004, MNRAS, 352, 1180

Filippenko A. V., Ho L. C., 2003, ApJ, 588, L13

Franx M., van Gorkom J. H., de Zeeuw P. T., 1994, ApJ, 436, 642

Friedli D., Benz W., 1993, A&A, 268, 65

García-Lorenzo B., Mediavilla E., Arribas S., del Burgo C., 1997, ApJ, 483, L99

García-Lorenzo B., Mediavilla E., Arribas S., 1999, ApJ, 518, 190

Helfer T. T., Blitz L., 1995, ApJ, 450, 90

Heller C. H., Shlosman I., 1994, ApJ, 424, 84

Hernandez O., Wozniak H., Carignan P., Amram P., Chemin L., Daigle O., 2005, ApJ, 632, 253

Knapen J. H., Shlosman I., Peletier R. F. 2000, ApJ, 529, 93

Laine S., Shlosman I., Knapen J. H., Peletier R. F., 2002, ApJ, 567, 97

Maciejewski W., Teuben P. J., Sparke L. S., Stone J. M., 2002, MNRAS, 329, 502

Maia M. A. G., Machado R. S., Willmer C. N. A., 2003, AJ, 126, 1750

Malkan M. A., Gorgian V., Tam R., 1998, ApJS, 117, 25

Márquez I., Masegosa J., Durret F., González Delgado R. M., Moles M., Maza J., Pérez E., Roth M., 2003, A&A, 409, 459

Masset F., Tagger M., 1997, A&A, 322, 442

Moellenhoff C., Matthias M., Gerhard O. E., 1995, A&A, 301, 359

Moles M., Márquez I., Pérez E., 1995, ApJ, 438, 604

Mulchaey J. S., Regan M. W., 1997, ApJ, 482, L135

Mundell C. G., Shone D. L., 1999, MNRAS, 304, 475

Muxlow T. W. B., Pedlar A., Holloway A. J., Gallimore J. F., Antonucci R. R. J., 1996, MNRAS, 278, 854

Nelson C. H., Whittle M., 1995, ApJS, 99, 67

Nelson C. H., Whittle M., 1996, ApJ, 465, 96

Peletier R. F., Knapen J. H., Shlosman I., Pérez-Ramírez D., Nadeau D., Doyon R., Rodriguez Espinosa J. M., Pérez García A. M., 1999, ApJS, 125, 363

Pérez E., Márquez I., Marrero I., Durret F., González Delgado R. M., Masegosa J., Maza J., Moles M., 2000, A&A, 353, 893

Pfenniger D., Friedli D., 1993, A&A, 270, 561

Pogge R. W., 1988, ApJ, 328, 519

Rand R. J., Wallin J. F., 2004, ApJ, 614, 142 (RW04)

Rand R. J., Lord S. D., Higdon J. L., 1999, ApJ, 513, 720

Rautiainen P., Salo H., Laurikainen E., 2002, MNRAS, 337, 1233

Rousset A., 1992, PhD thesis, Univ. J. Monnet de Saint-Etienne

Sakamoto K., Okumura S. K., Ishizuki S., Scoville N. Z., 1999, ApJ, 525, 691

Schinnerer E., Eckart A., Tacconi L. T., Genzel R., Downes D., 2000, ApJ, 533, 850 (S+00)

Schoenmakers R. H. M., Franx M., de Zeeuw P. T., 1997, MNRAS, 292, 349

Schwarz M. P., 1981, ApJ, 247, 77

Schwarz M. P., 1984, A&A, 133, 222

Scoville N. Z., Matthews K., Carico D. P., Sanders D. B., 1988, ApJ, 327, L61

Shapiro K. L., Gerssen J., van der Marel R. P., 2003, AJ, 126, 2707 (Sh+03)

Sheth K., Vogel S. N., Regan M. W., Teuben P. J., Harris A. I., Thornley M. D., 2002, AJ, 124, 2581

Thronson H. A. et al., 1989, ApJ, 343, 158

Tremaine S., Weinberg M. D., 1984, ApJ, 282, L5

Vazdekis A., 1999, ApJ, 513, 224

Wada K., Norman C. A., 2002, ApJ, 566, L21

Wong T., Blitz L., Bosma A., 2004, ApJ, 605, 183

Wozniak H., Combes F., Emsellem E., Friedli D., 2003, A&A, 409, 469

Yuan C., Kuo C.-L., 1998, ApJ, 497, 689

de Zeeuw P. T. et al., 2002, MNRAS, 329, 513

This paper has been typeset from a TEX/LATEX file prepared by the author.